

Article

# Multi-Stage Introduction of Precious and Critical Metals in Pyrite: A Case Study from the Konos Hill and Pagoni Rachi Porphyry/Epithermal Prospects, NE Greece

Constantinos Mavrogonatos <sup>1,\*</sup>, Panagiotis Voudouris <sup>1</sup>, Federica Zaccarini <sup>2</sup>,  
Stephan Klemme <sup>3</sup>, Jasper Berndt <sup>3</sup>, Alexandre Tarantola <sup>4</sup>, Vasilios Melfos <sup>5</sup> and  
Paul G. Spry <sup>6</sup>

<sup>1</sup> Faculty of Geology and Geoenvironment, National and Kapodistrian University of Athens, 15784 Athens, Greece; voudouris@geol.uoa.gr

<sup>2</sup> Department of Applied Geosciences and Geophysics, University of Leoben, 8700 Leoben, Austria; federica.zaccarini@unileoben.ac.at

<sup>3</sup> Institut für Mineralogie, Westfälische-Wilhelms Universität Münster, 48149 Münster, Germany; stephan.klemme@uni-muenster.de (S.K.); jberndt@uni-muenster.de (J.B.)

<sup>4</sup> Université de Lorraine, CNRS, GeoRessources, F-54000 Nancy, France; alexandre.tarantola@univ-lorraine.fr

<sup>5</sup> Faculty of Geology, Aristotle University of Thessaloniki, 54124 Thessaloniki, Greece; melfosv@geo.auth.gr

<sup>6</sup> Department of Geological and Atmospheric Sciences, Iowa State University, Ames, IA 50011-1027, USA; pgspry@iastate.edu

\* Correspondence: kmavrogon@geol.uoa.gr; Tel.: +30-210-727-4794

Received: 13 July 2020; Accepted: 4 September 2020; Published: 5 September 2020



**Abstract:** The Konos Hill and Pagoni Rachi porphyry-epithermal prospects in northeastern Greece are characterized by abundant pyrite that displays important textural and geochemical variations between the various ore stages. It is commonly fine-grained and anhedral in the porphyry-related mineralization (M- and D-type veins), while it forms idiomorphic, medium- to coarse-grained crystals in the late, epithermal style veins (E-type). Porphyry-style pyrite from both prospects is characterized by an enrichment in Co, Se, Cu, and minor Zn, and a depletion in other trace elements, like Bi, Mo, Ag, etc. Pyrite in epithermal-style mineralization is mostly characterized by the presence of As, Bi, Pb, Ni, and Se. Gold in pyrite from all mineralization stages occurs as a non-stoichiometric substituting element, and its abundance correlates with As content. Arsenic in pyrite from Konos Hill records an increase from the porphyry stage to the epithermal stage (along with gold); however, at Pagoni Rachi, the highest Au and As contents are recorded in D-type pyrite and in the epithermal stage. The composition of the studied pyrite marks changes in the physico-chemical conditions of the ore-forming fluids and generally follows the geochemical trends from other porphyry-epithermal systems elsewhere. However, a notable enrichment of Se in the porphyry-style pyrite here is a prominent feature compared to other deposits and can be considered as an exploration tool towards Au-enriched mineralized areas.

**Keywords:** pyrite; trace elements; LA-ICP-MS; critical metals; porphyry-epithermal; exploration; Greece

## 1. Introduction

Pyrite is the most common sulfide mineral in the Earth's crust and is generally common in most ore deposit types [1–4]. Its ideal chemical composition, as expressed by the formula FeS<sub>2</sub>, is not common in nature, as natural pyrites always contain small quantities of various elements beyond the essential

Fe and S [1]. Thus, pyrite has attracted attention as a potential vector to identify fertile ore zones, as it may contain a large budget of trace elements including Au, Ag, Cu, Pb, Zn, Co, Ni, As, Sb, Se, Te, Hg, Tl, Bi, and PGE, some of which can reach concentrations of up to a few weight-percent [2,3,5–7]. In such cases, pyrite may contain an economically exploitable source for these metals [8–10].

Trace elements may be present in pyrite, as nano-sized inclusions (or nanoparticles, e.g., [11,12]) or as non-stoichiometric substitutions in its structure [5,13,14]. Arsenic is one of the most incorporated elements into pyrite, reaching concentrations in the range of major elements (almost up to 10 wt.%, e.g., [15,16]) and is commonly associated with gold mineralization [3,11,14,17].

The composition of pyrite has emerged as an indicator of ore-forming processes, including knowledge of the transport and depositional mechanisms of precious and critical elements in hydrothermal systems [3–7,10,18–20]. The chemistry of pyrite is highly dependent on the hydrothermal processes responsible for its deposition, which may fractionate trace elements between the vapor, liquid, and solid phases [21–23]. This means that its composition is mainly a function of the physicochemical features of the precipitating fluid including pH, temperature, redox, and the availability of complex-forming ligands [3,4,7,10,13,24]. Fluid-wall rock interaction, the composition of the host rocks, and phase separation also affect the chemical signature of pyrite [4,7,10,18,25]. However, elements enriched in the host rocks are not necessarily leached by the associated hydrothermal fluids [26].

In deposits where pyrite is a major Au carrier (e.g., orogenic-Au and Carlin-style deposits), the trace element content of pyrite has been well studied, owing to its economic significance. This has provided constraints on the mineral/fluid partitioning of such elements, and the saturation state of the parental hydrothermal solutions [2,27,28]. However, this is not the case with porphyry deposits, where only a relatively small number of studies have been conducted [3,6,19,29–33]. The trace element geochemistry of pyrite in the transition from the porphyry to epithermal environment remains poorly constrained [19,20].

Pyrite is a common mineralogical constituent in numerous ore deposits and prospects in Greece; however, the study of its trace element geochemistry is limited. In this paper, we use laser ablation-inductively coupled plasma-mass spectrometry (LA-ICP-MS) analyses to evaluate the composition of various generations of pyrite in two neighboring porphyry-epithermal systems in northeast (NE) Greece: The Konos Hill and Pagoni Rachi prospects. The trace element composition of pyrite is used to identify possible relationships between the metal endowment of the hydrothermal fluids, from which pyrite precipitated, and to elucidate any physicochemical changes that occurred as the ore forming system evolved. Finally, we make a comparison to analogous porphyry/epithermal deposits elsewhere and try to determine chemical fingerprints in the various generations of pyrite, which could point towards ore-grade mineralized events and/or zones. This could potentially be used as an exploration tool for other similar deposits and prospects in Greece and elsewhere.

## 2. Materials and Methods

Forty-five polished sections of sulfide mineralization were studied with an optical microscope and a JEOL JSM 5600 scanning electron microscope equipped with back-scattered imaging capabilities, at the Department of Mineralogy and Petrology, University of Athens, Athens, Greece. The chemical composition of sulfides from selected sections was carried out using a JEOL JXA 8200 Superprobe electron-microprobe at the “Eugen F. Stumpfl” Laboratory, Leoben University, Leoben, Austria. The operating conditions were accelerating voltage 20 kV, beam current 10 nA, beam size  $\approx 1 \mu\text{m}$ . Counting times were 20 s on the peak and 10 s on the backgrounds for major elements. The counting times were increased to 60 s and 30 s for peak and backgrounds, respectively, when analyzing the trace elements. The following X-ray lines were used: AsL $\alpha$ , AuL $\alpha$ , SeL $\alpha$ , CuK $\alpha$ , FeK $\alpha$ , PbM $\alpha$ , SK $\alpha$ , SbL $\alpha$ , NiK $\alpha$ , CoK $\alpha$ , and ZnK $\alpha$ . The standards were: synthetic GaAs for As (detection limit 350 ppm), synthetic electrum for Au (detection limit 100 ppm), synthetic AgBiSe<sub>2</sub> for Se (detection limit 200 ppm), chalcopyrite for Cu (detection limit 150 ppm), pyrite for S and Fe (detection limit 150 ppm), galena for

Pb (detection limit 700 ppm), stibnite for Sb (detection limit 350 ppm), skutterudite for Co (detection limit 150 ppm), millerite for Ni (detection limit 150 ppm), and sphalerite for Zn (detection limit 400 ppm).

Laser ablation-ICP-MS analyses of the same samples were conducted at the Institute of Mineralogy, University of Münster, Germany, with a pulsed 193 nm ArF excimer laser (Analyte G2, Photon Machines). Pre-defined (by optical and electron microscopy, as to avoid any visible inclusions) areas of the polished sections were ablated using a 35 µm-sized spot diameter. A repetition rate of 10 Hz and an energy of ~4 J/cm<sup>2</sup> were used throughout the session. The laser system was coupled to an Element 2 mass spectrometer (ThermoFisher). Forward power was 1250 W and reflected power <1 W, gas flow rates were 1.2 L/m for He carrier gas, 0.9 L/m and 1.2 L/m for the Ar-auxiliary and sample gas, respectively. The argon cooling gas flow rate was set to 16 L/min. Before starting an analysis, the system was calibrated to a NIST 612 reference glass measuring <sup>139</sup>La, <sup>232</sup>Th and <sup>232</sup>Th<sup>16</sup>O to get stable signals and high sensitivity, as well as low oxide rates (<sup>232</sup>Th<sup>16</sup>O/<sup>232</sup>Th < 0.1%) during ablation. A total of 20 elements (<sup>55</sup>Mn, <sup>59</sup>Co, <sup>60</sup>Ni, <sup>63</sup>Cu, <sup>66</sup>Zn, <sup>69</sup>Ga, <sup>73</sup>Ge, <sup>75</sup>As, <sup>77</sup>Se, <sup>95</sup>Mo, <sup>107</sup>Ag, <sup>111</sup>Cd, <sup>115</sup>In, <sup>118</sup>Sn, <sup>121</sup>Sb, <sup>182</sup>W, <sup>197</sup>Au, <sup>205</sup>Tl, <sup>208</sup>Pb, and <sup>209</sup>Bi) were quantitatively analyzed using the NIST 610 glass as an external standard. Iron, previously determined by EPM analyses, was used as the internal standard. The run time of the single ablation pattern was 60 s (20 s for background, 40 s for peak after switching the laser on). Concentrations of measured elements were calculated using the Glitter software [34,35], and a signal spike filter was applied if necessary. Standard reference material MASS-1 was analyzed in order to monitor for precision and accuracy. Despite the different matrix between silicate standard and sulfide sample obtained results generally match the published range of concentrations, given in the GeoReM database (version 23 [36]) (see Supplementary Table S1). This indicates the trace element concentrations in natural pyrite samples could be analyzed reliably by LA-ICP-MS. Average detection limits for the analyzed elements are as follows (in ppm): Mn = 0.8, Co = 0.3, Ni = 4, Cu = 0.5, Zn = 4, Ga = 0.2, Ge = 1.3, As = 1.9, Se = 5.6, Mo = 0.15, Ag = 0.8, Cd = 0.8, In = 0.06, Sn = 0.3, Sb = 0.19, W = 0.04, Au = 0.04, Tl = 0.02, Pb = 0.06, Bi = 0.03. All numbers are reported as determined, regardless of the number of significant digits.

### 3. Geological Setting

#### 3.1. Regional Geology

The Rhodope Massif occupies an important part of northern Greece and exhibits a complex tectonometamorphic evolution (e.g., [37]). It comprises three sub-domains the [38,39]: (1) Northern Rhodope Domain; (2) Southern Rhodope Core Complex (including the Kerdylion unit of the former Serbo-Macedonian Massif); and (3) Chalkidiki Block. The Northern Rhodope Domain occupies a major part of NE Greece (Figure 1) and is further divided into three units. The structurally lower unit comprises a gneissic Paleozoic basement, subdivided into three migmatitic domes (Arda, Biala Reka-Kechros, and Kesebir-Kardamos). The intermediate unit consists of high-grade metamorphic basement rocks, and the structurally upper unit, known as the Circum-Rhodope Belt, comprises a thrust system of NW-trending sub-units (e.g., the Makri sub-unit), composed of low grade metamorphic rocks, including the Evros ophiolites [40–42]. Sequences of thick clastic rocks are also widespread in NE Greece (Figure 1) and are deposited in E-W trending, structurally controlled basins [43,44], where voluminous mafic to felsic magmatic rocks with a pronounced post-subduction signature, also occur [45–47].

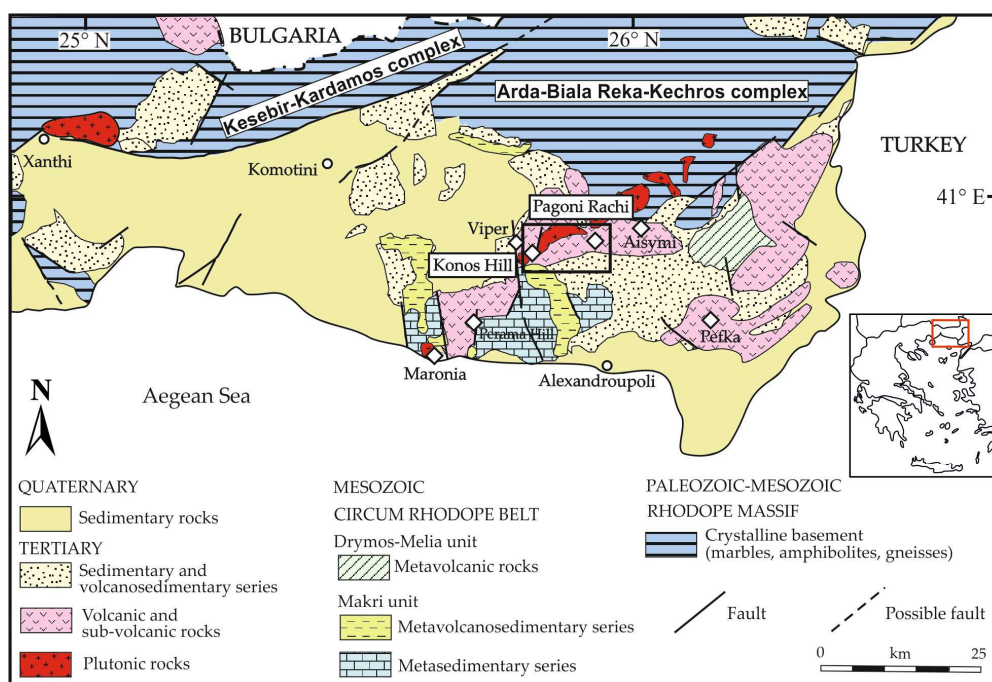


**Figure 1.** Simplified geological map of northeast (NE) Greece (after Voudouris et al. [48]; Mavrogonatos et al. [49]) showing the most important porphyry-epithermal deposits and prospects in the area. The black box marks the location of the study area.

The magmatic rocks vary in age from Eocene to Miocene and are characterized by calc-alkaline to shoshonitic and ultra-potassic affinities [45,47,50–52]. Widespread hydrothermal activity resulted in the formation of important mineralization, mainly in the Rhodope (Western Thrace), and to a lesser extent the Serbo-Macedonian (Chalkidiki) domains [46,51,53–56].

Among the various types of mineralization, many porphyry- and epithermal-style occurrences (Figure 1) display enrichment in several elements including Au, Ag, Mo, Re, Te, Se, In, Ga, Ge, and Bi. (e.g., [55]). Porphyry-style mineralization in Western Thrace include the Aisymi-Leptokaria porphyry Mo [57], and a number of Cu-Mo-Re-Au systems, namely the Maronia [58,59], Konos Hill (e.g., [49,60–62]), and Pagoni Rachi prospects (e.g., [63–67]). Important examples of epithermal-style mineralization in West Thrace (Figures 1 and 2) include the Viper (e.g., [68–70]) and Perama Hill [71] Au-Ag-Cu deposits, as well as the Achla Tarla, St. Philippos, and Pefka [55,72] polymetallic deposits.

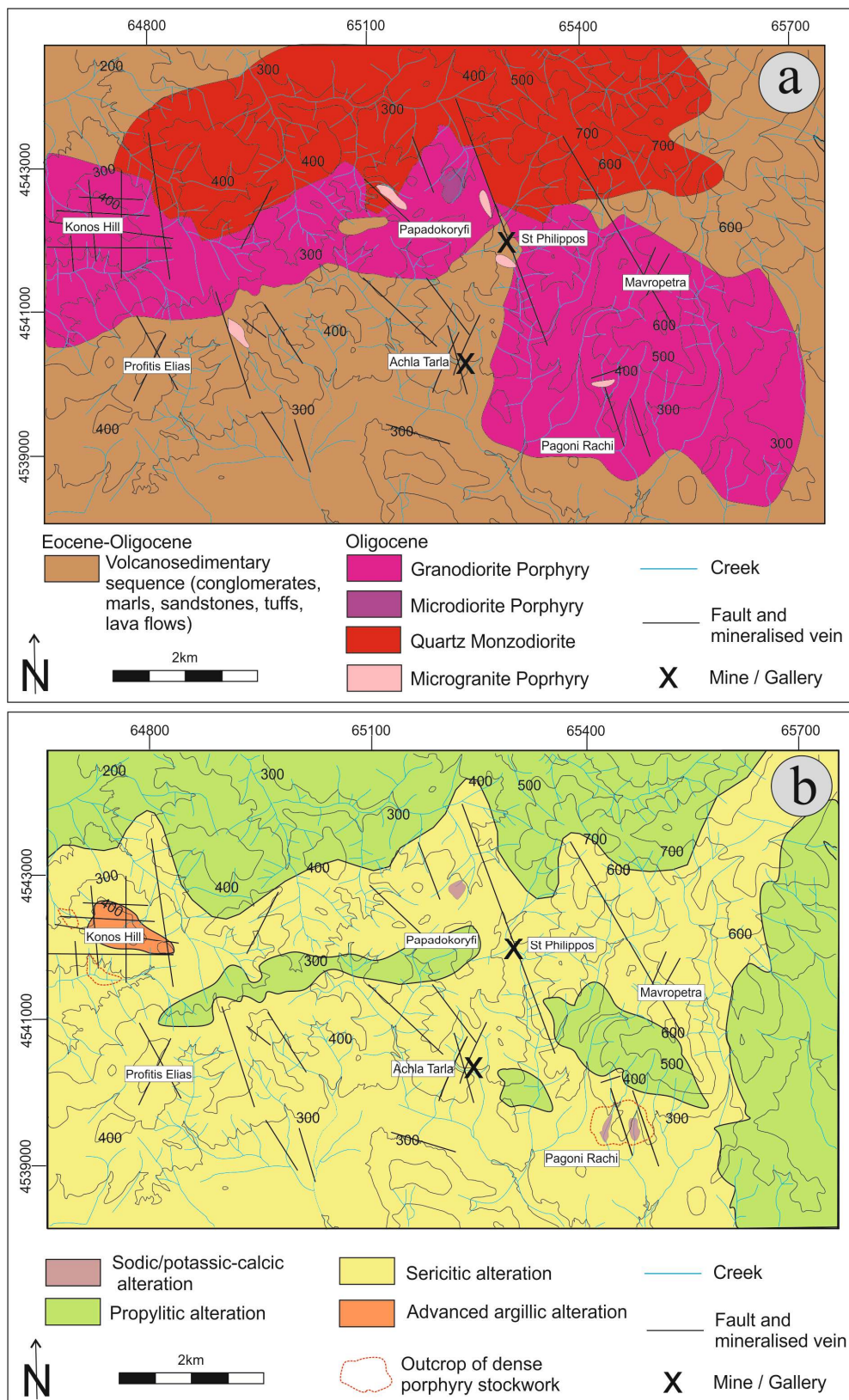


**Figure 2.** Geological (a) and alteration (b) map showing the location of the Konos Hill and Pagoni Rachi porphyry-epithermal prospects, among other mineralization occurring in the Sapes-Kirki area.

### 3.2. Geology and Mineralization of the Studied Prospects

In the central part of the West Thrace metallogenic province, lies the Sapes-Kirki area, which mainly comprises conglomerates, marls, sandstones, and volcanoclastic material (e.g., tuffs) of Priabonian age (Figure 2). The sequence was intruded by four types of subvolcanic rocks with subalkaline to alkaline affinities that form stocks and dikes [53]. These rocks are, from oldest to youngest, based on cross-cutting relations: hornblende-biotite granodiorite porphyry, pyroxene-biotite microdiorite porphyry, quartz monzodiorite, and microgranite porphyry [61,73].

Radiometric ages for the granodiorite porphyry are  $32.6 \pm 0.5$  Ma ( $^{40}\text{Ar}/^{39}\text{Ar}$  on biotite, [73]), for the monzodiorite,  $31.9 \pm 0.5$  Ma (Rb/Sr on biotite, [45]) and  $32.05 \pm 0.07$  (U-Pb zircon, [47]). The hornblende-biotite granodiorite porphyry occupies a major part of the study area and forms an E-trending elongated stock that hosts both the Konos and the Pagoni Rachi porphyry-epithermal prospects (Figure 2). The northernmost part of the area is dominated by quartz monzodiorite, while a small body of pyroxene-biotite microdiorite occurs north of the Papadokoryfi Hill. Small bodies of microgranite porphyry are scattered throughout the area, emplaced mainly along NNW-trending fault zones. Most of the rocks underwent intense hydrothermal alteration (Figure 2b) [48,49,55,61,62,64–67,69,70]. The tectonic regime in the area comprises four major fault directions: N-S, E-W, ENE-WSW and NNW-SSE, with the last being associated with major ore-bearing structures, which, for example, hosts the St Philippos polymetallic deposit [65].

#### 3.2.1. The Konos Hill Prospect

The Konos Hill porphyry-epithermal prospect comprises quartz porphyry stockworks, hosted in the intensively altered granodiorite porphyry, set in an NNW-trending direction (Figure 2), [49,61,62]. The veins are sinuous to planar and banded, a feature that was recently found to characterize quartz veins from several porphyry Cu-Mo-Re-Au systems in northeastern Greece [55,74]. The main metallic minerals are pyrite, molybdenite, rheniite, chalcopyrite along with minor bornite, enargite, colusite, and tetrahedrite/tennantite [48,55,60,64–67], and are associated with sodic/potassic alteration of the host granodiorite. Pyrite veins, associated with widespread sericitic alteration, overprint the quartz stockwork mineralization. They usually form stockworks (now mostly oxidized), but also fill the centerlines of early quartz veins. At the higher topographic levels of the system (on top of Konos Hill), advanced argillic alteration assemblages occur mostly along N- and E-trending faults, leading to partial telescoping of the porphyry system. They comprise pyrophyllite, diaspore, zunyite, alunite, and aluminum-phosphates-sulphates (APS), associated with oxidized mineralization [49,60–62]. Peripheral to the system, quartz-calcite veins (E-type) with base metals and epithermal affinities occur. They are associated with lateral sericitic (and minor argillic) alteration, dominated by quartz, sericite, calcite ( $\pm$  kaolinite) and comprise mostly pyrite, sphalerite, galena, and tetrahedrite/tennantite group minerals (Table 1).

**Table 1.** Typology and alteration characteristics of pyrite-bearing mineralization stages analyzed in the present study, from the Konos Hill and Pagoni Rachi porphyry/epithermal prospects.

Prospect	Vein Type	Vein Assemblage	Alteration Assemblage	Form, Texture, Zonation
Konos Hill	D-type	Qz + Py + Ccp ± Mol + Bn + Po + Hem + Ser	Ser + Qz ± Py ± Cal ("Sericitic")	Continuous quartz-pyrite veins/pyrite-chalcopyrite-molybdenite veins reopening and overprinting earlier quartz veins
	"Epithermal" (E-type)	Qz + Cal + Sp + Gn + Py + Ccp ± Tnt/Ttr ± Eng ± Ag-Au	Qz + Cal + Ser ± Kln	Continuous straight-sided, up to 15 cm wide, quartz-carbonate veins with sharp parallel walls
Pagoni Rachi	M-type	Mag + Ccp + Hem + Py + Bn + Or/Ab + Bt + Act + Ep + Mol + Au	Qz + Or/Ab + Act + Ep + Bt + Chl + Cal + Mag ("Sodic/Potassic-Calcic")	Narrow (width less than 0.5 cm), irregular in shape and discontinuous and/or straight-sided veinlets
	D-type	Py + Ccp ± Mol + Po + Hem + Ser ± Qz ± Au + Cal ± Rhn ± Bn ± Gn	Qz + Ser + Py ± Cal ("Sericitic")	Continuous, up to 10 cm wide, massive pyrite veins, pyrite-molybdenite-chalcopyrite veins, reopening and overprinting earlier quartz veins
	"Epithermal" (E-type)	Qz + Cal + Sp + Gn + Ccp + Py ± Tnt/Ttr ± Eng ± Ag-Au ± Tell ± Ser ± Kln	Qz + Cal + Ser ± Kln	Continuous straight-sided, up to 20 cm wide, quartz-carbonate veins with sharp parallel walls

Abbreviations: Act = actinolite, Ab = albite, Ag-Au = gold-silver alloy, Au = native gold, Bn = bornite, Bt = biotite, Cal = calcite, Chl = chlorite, Ccp = chalcopyrite, Ep = epidote, Eng = enargite, Gn = galena, Hem = hematite, Kln = kaolinite, Mag = magnetite, Mol = molybdenite, Or = orthoclase, Py = pyrite, Po = pyrhotite, Rhn = Rheniite, Qz = quartz, Ser = sericite, Sp = sphalerite, Tell = tellurides, Tnt = tennantite, Ttr = tetrahedrite.

### 3.2.2. The Pagoni Rachi Prospect

The Pagoni Rachi telescoped porphyry-epithermal prospect is hosted in a similar granodiorite porphyry stock like that at Konos Hill. The mineralization occurs as a very dense quartz stockwork, associated with extensive hydrothermal alteration [63,65–67]. The Pagoni Rachi system exhibits an unusual enrichment in Re, expressed by high concentrations of Re in molybdenite and by the presence of the rare sulfide rheniite [63–65]. The core of the system is dominated by sodic/potassic-calcic alteration associated with magnetite and quartz veins, as well as sodic/potassic alteration related to banded quartz-molybdenite veins. Massive pyrite veins associated with sericite-carbonate alteration overprint earlier alteration and mineralization. Epithermal-style veins (E-type) commonly set in a N- and NW-trending direction, locally overprint the porphyry mineralization. They are related to argillic alteration assemblages and carry base metal sulfides (pyrite, sphalerite galena) as well as precious metals (Ag-Au alloy) and a suite of sulfosalts and tellurides (Table 1) [55,65].

## 4. Results

Vein terminology used hereafter in this paper is based on Arancibia and Clark [75] for M-type veins, Gustafson and Hunt [76] and Seedorff et al. [22] for A-, D-type veins, and Masterman et al. [77], Voudouris et al. [65], and Monecke et al. [78] for E-type veins. The vein characteristics, as well as their mineralogical and textural features are summarized in Table 1.

### 4.1. Occurrence and Textural Features of Pyrite

Pyrite is a common constituent of the Konos Hill prospect and is the dominant mineral in D-type veins, which form stockworks, and is associated with sericitic alteration of the host granodiorite porphyry (Figure 3a–c). Sericitic (or "phyllitic") alteration is the most widespread type in the area

and caused pervasive obliteration of pre-existing, sodic±potassic alteration assemblages (e.g., albite, K-feldspar, biotite, chlorite). The D-type pyritic veins (up to 5 cm wide) are mostly oxidized with pyrite filling centerlines associated with reopening of A-type, quartz-stockwork veins (Figure 3b,c). Pyrite in D-type veins is usually fine- to medium-grained (from a few  $\mu\text{m}$ , up to 0.5 cm) and is characterized by a porous texture. Its grain shape is anhedral and displays a characteristic “corroded” rim. Pyrrhotite (Figure 4b), and less commonly chalcopyrite, occurs as inclusions. Molybdenite is in places associated with chalcopyrite and pyrite, disseminated in the sericitic-altered granodiorite or in the quartz veins (Figure 4c). In addition, molybdenite forms fine-grained aggregates (up to 100  $\mu\text{m}$  in length) that develop in the grain boundaries of pyrite (Figure 5a). Bornite, magnetite, enargite, and colusite also accompany pyrite, but occur in trace amounts (see also Voudouris et al. [48,49,60,62,65]).

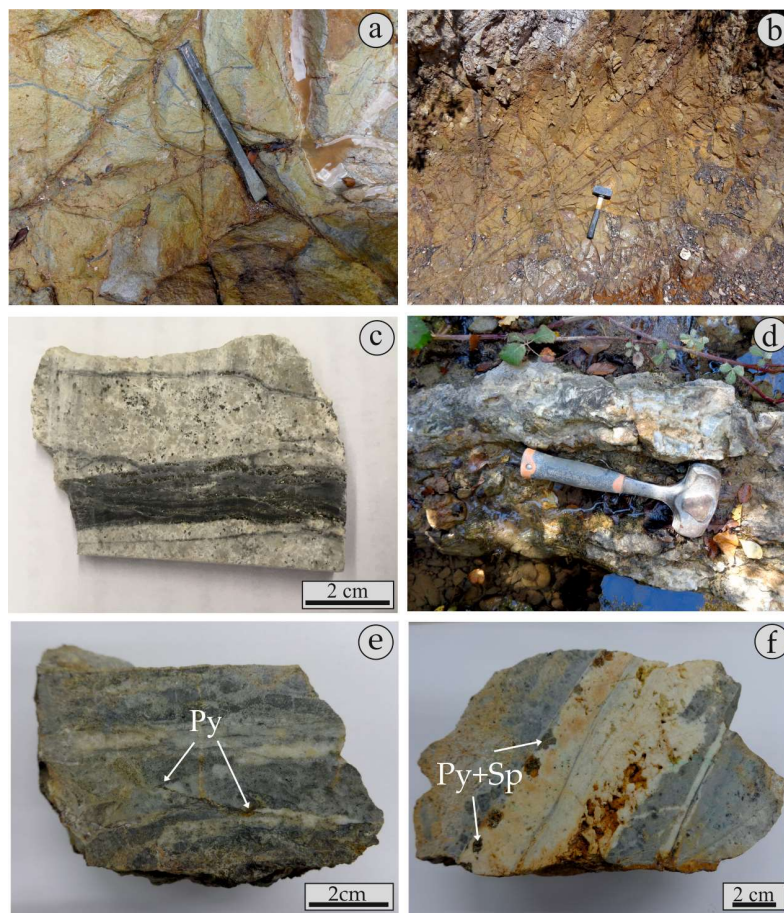


**Figure 3.** Field and hand-specimen photographs of pyrite-bearing ores from the Konos Hill porphyry-epithermal prospect: (a) Oxidized D-type veins crosscutting sericitic-altered granodiorite porphyry; (b,c) Surface outcrop of quartz stockwork veins crosscutting sericitic-altered granodiorite porphyry. Note in c that pyrite is mostly deposited along center lines of the quartz veins (sample KMSP64); (d) NNE-trending, epithermal-style, milky quartz-calcite vein (E-type) associated with quartz-sericite-calcite alteration of the host granodiorite porphyry; (e) Hand specimen with pyrite (Py) from the quartz-calcite vein shown in (d) (sample KMSP48); (f) Epithermal-style, quartz-calcite (E-type) vein with pyrite (Py) and sphalerite (Sp), (sample KMSP78).

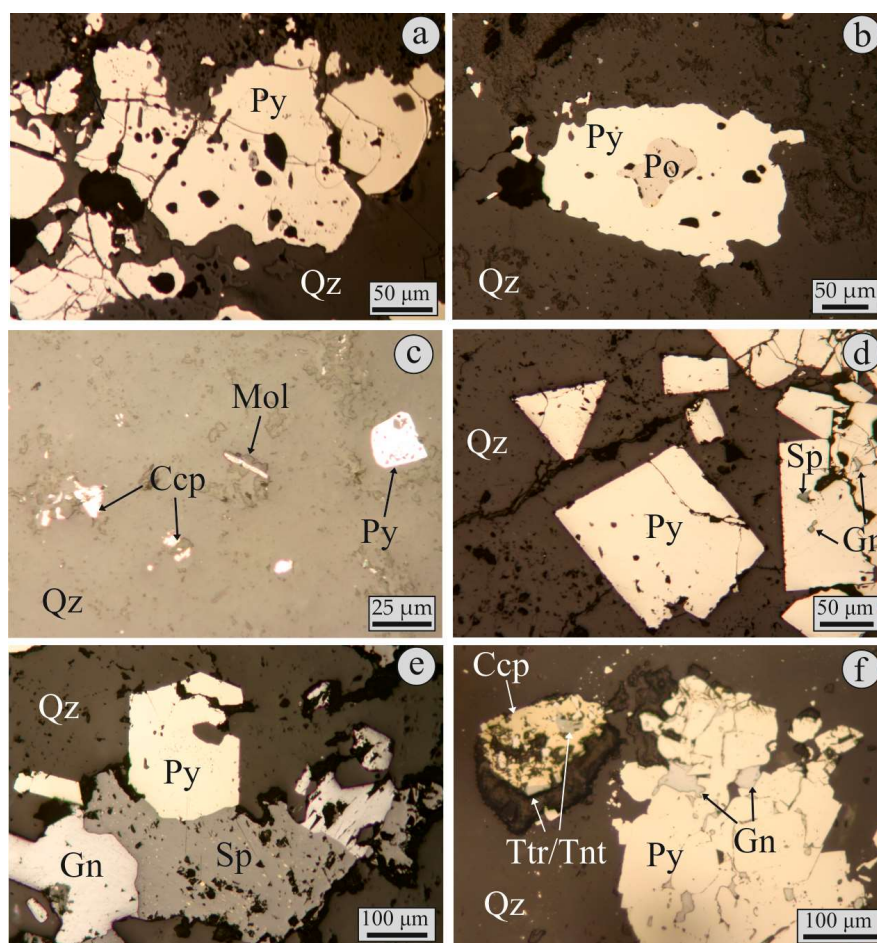


**Figure 4.** Reflected light photomicrographs of pyrite and associated opaque minerals from different stages mineralization in the Konos Hill porphyry-epithermal prospect. (a) Anhedra, “corroded” pyrite (py) grains in quartz (Qz), from a D-type vein (Sample KMSP64); (b) Anhedra, “corroded” pyrite grain including pyrrhotite (Po), D-type vein (Sample KMSP64); (c) Disseminated molybdenite (Mol) in association with chalcopyrite (Ccp) and pyrite (Py) in quartz (Qz), D-type vein, (Sample KMSP64); (d) Euhedral pyrite (py) in quartz (Qz) that includes blebs of sphalerite (Sp) and galena (Gn), epithermal-style vein, (sample KMSP48); (e) Euhedral pyrite (py) associated with galena (Gn) and sphalerite (Sp), the latter displaying “chalcopyrite disease”, within quartz (Qz), E-type vein (KMSP48); (f) Euhedral pyrite rimmed by and including galena (Gn), in association with an intergrowth of chalcopyrite (Ccp) and tetrahedrite-tennantite group mineral (Ttr/Tnt), included in quartz (Qz), E-type vein (KMSP48).

Pyrite is also widespread in epithermal-style (E-type) veins that crosscut/overprint the porphyry-style mineralization. These veins, most of which occur along NNW-, and E-trending directions, are composed of quartz and calcite (Figure 3d–f) and display minor banding. The veins are of high- to intermediate-sulfidation affinities [49,55] and are associated with argillic (and less commonly advanced argillic) alteration. In these veins, pyrite forms euhedral crystals that are up to 1 cm in size, which are commonly isolated, included in quartz and/or calcite, or they form aggregates. They are commonly associated with Fe-poor sphalerite, galena, chalcopyrite, and tetrahedrite-tennantite group minerals (Figure 4d,e). Galena forms euhedral to subhedral grains, spatially associated with sphalerite and pyrite (Figure 4e), or it occurs interstitially between pyrite grains (Figure 4f). It can also form swarms of inclusions that commonly occur along growth zones of the host pyrite crystal (Figure 5b). Sphalerite usually contains tiny inclusions of chalcopyrite (chalcopyrite “disease”, Figure 4e).

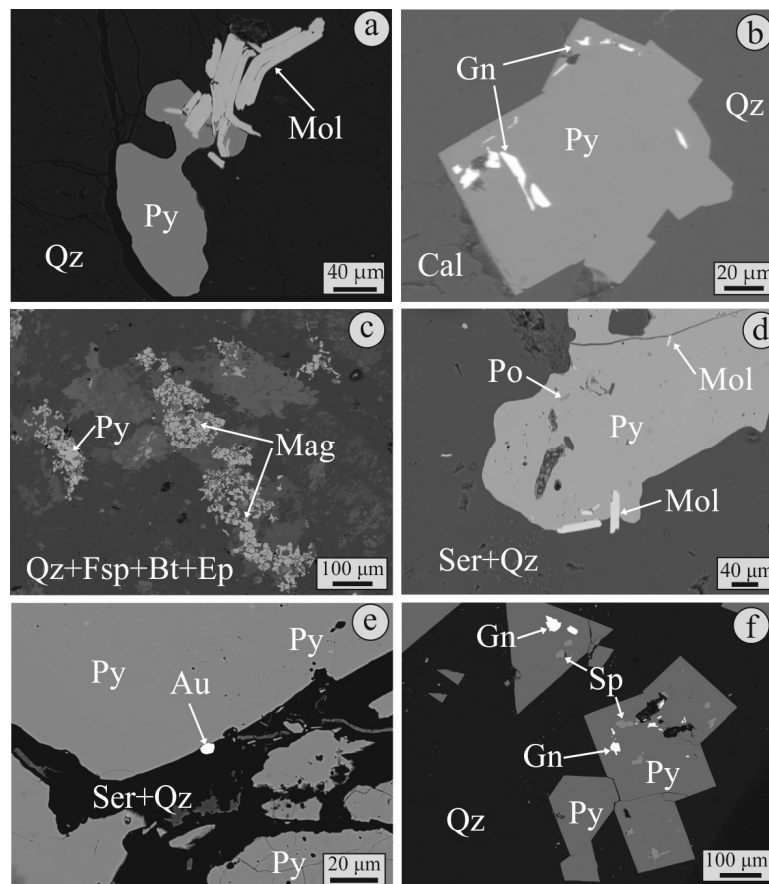


**Figure 5.** SEM back-scattered electron images of pyrite-bearing assemblages. (a) Intergrowth of pyrite (Py) and molybdenite (Mol) in quartz (Qz), D-type vein, Konos Hill prospect (sample KMSP64); (b) Euhedral pyrite (Py) that includes galena (Gn) in quartz (Qz) and calcite (Cal), epithermal style vein, Konos Hill prospect (sample KMSP48); (c) Magnetite (Mag) with pyrite (Py) associated with quartz (Qz)—feldspar (Fsp, orthoclase and/or albite)—biotite (Bt)—epidote (Ep) altered granodiorite porphyry, M-type vein, Pagoni Rachi prospect (sample KMSP74); (d) Pyrite (Py) including minor pyrrhotite and associated with molybdenite (Mol), in sericite (Ser) and quartz (Qz) altered granodiorite porphyry, D-type vein, Pagoni Rachi prospect (sample KMSP66); (e) Native gold (Au) in association with pyrite (Py) in a sericite (Ser) and quartz (Qz) matrix, D-type vein, Pagoni Rachi prospect (sample KMSP66); (f) Euhedral pyrite (Py) crystals in quartz (Qz) and including galena (Gn) and sphalerite (Sp), E-type vein, Pagoni Rachi prospect (sample KMSP53).

In the Pagoni Rachi mineralization, pyrite is widespread and occurs throughout the paragenetic sequence [65]. Pyrite is found in: (i) early magnetite veins (M-type), (ii) D-type veins, and (iii) epithermal (E-type) veins.

Pyrite is a minor constituent of the early M-type veins. They are irregular in shape and discontinuous and are associated with the sodic/potassic-calcic alteration of the granodiorite porphyry (Figure 6a–c). They form a stockwork of veinlets up to 0.5 cm wide (Figure 6b,c) associated with variable amounts of secondary albite, orthoclase, biotite, actinolite, and chlorite. The M-type veinlets are commonly very narrow (less than 0.5 cm), and are dominated by very fine-grained, anhedral magnetite. The pyrite grains are also fine-grained (up to 100  $\mu\text{m}$ ) and are commonly anhedral in shape. They coexist with magnetite, chalcopyrite (Figures 5c and 7a,b), and minor amounts of bornite, gold, and molybdenite.

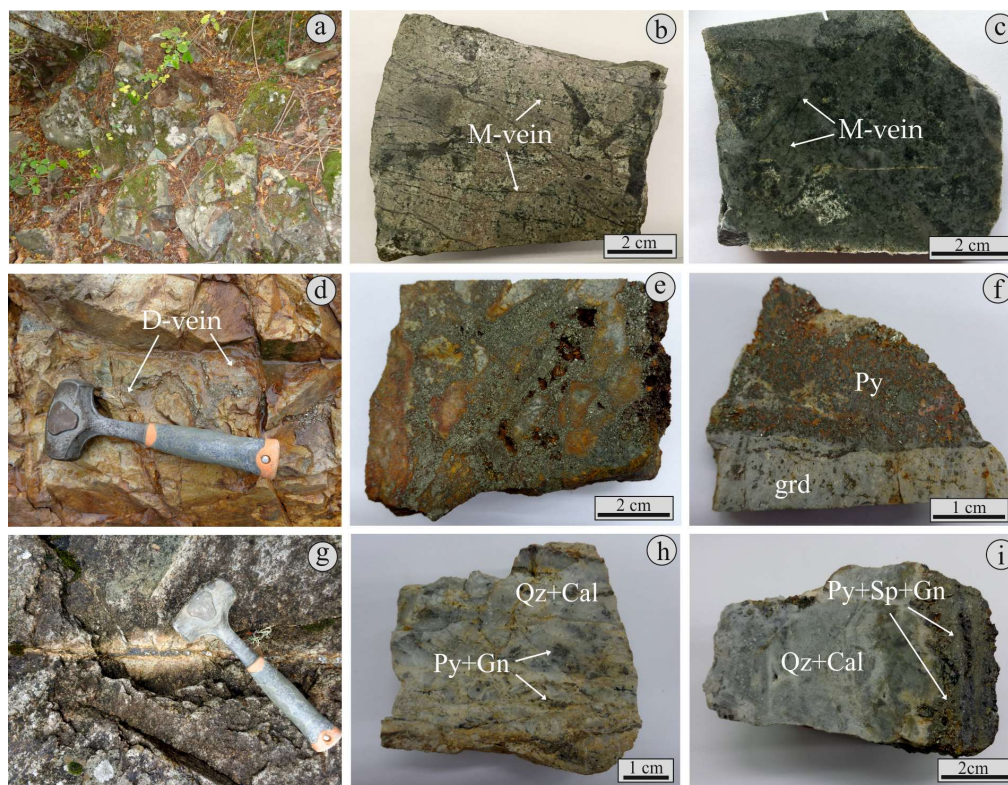


**Figure 6.** Field and hand-specimens photographs of pyrite-bearing rocks from the Pagoni Rachi porphyry/epithermal prospect: (a) Sodic/potassic-calcic altered granodiorite porphyry crosscut by magnetite veinlets; (b,c) Magnetite (M-type) veins crosscutting sodic/potassic-calcic altered granodiorite (samples KMPR74 and KMPR68, respectively); (d) D-type pyrite (py) vein crosscutting sericitic-altered granodiorite porphyry; (e–f) Massive pyrite vein (D-type), cementing fragments of sericitic altered granodiorite porphyry, grd = granodiorite (sample KMPR66); (g) Epithermal-style vein with sphalerite and pyrite, crosscutting sericitic-altered (sericite and calcite) granodiorite porphyry; (h,i) Hand specimens of epithermal-style, clear to milky quartz (Qz)—calcite (Cal) veins (E-type) with pyrite (Py), sphalerite (Sp) and galena (Gn) (samples KMPR53 and KMPR83, respectively).

The transitional porphyry to epithermal, D-type veins are very well developed in the Pagoni Rachi system and are the major carrier of Au in the system [65]. They form discontinuous planar to curvy veins that are up to 15 cm wide (Figure 6d–f). Pyrite occupies more than 90% of the vein, and is associated with strong sericitic (sericite, quartz, and calcite) alteration of the host rock which obliterated earlier alteration assemblages. Pyrite in D-type veins (Figure 7c–f) is massive and it forms anhedral grains up to 0.5 cm in size. Some brecciation is evident, and locally, pyrite grains are characterized by suture-like grain boundaries (Figure 7c). They commonly contain numerous, minute inclusions of pyrrhotite and/or chalcopyrite (Figure 7d–f). Pyrite is also spatially associated with molybdenite (Figure 7e). In such cases, molybdenite forms fine- to medium-grained aggregates composed of elongated crystals, and fills interstices (Figure 7e), or can be included in pyrite (Figure 5d). Fine-grained native gold (up to 15  $\mu\text{m}$  in size) occurs in fractures of pyrite crystals (Figure 7f), or along their margins (Figure 8e).

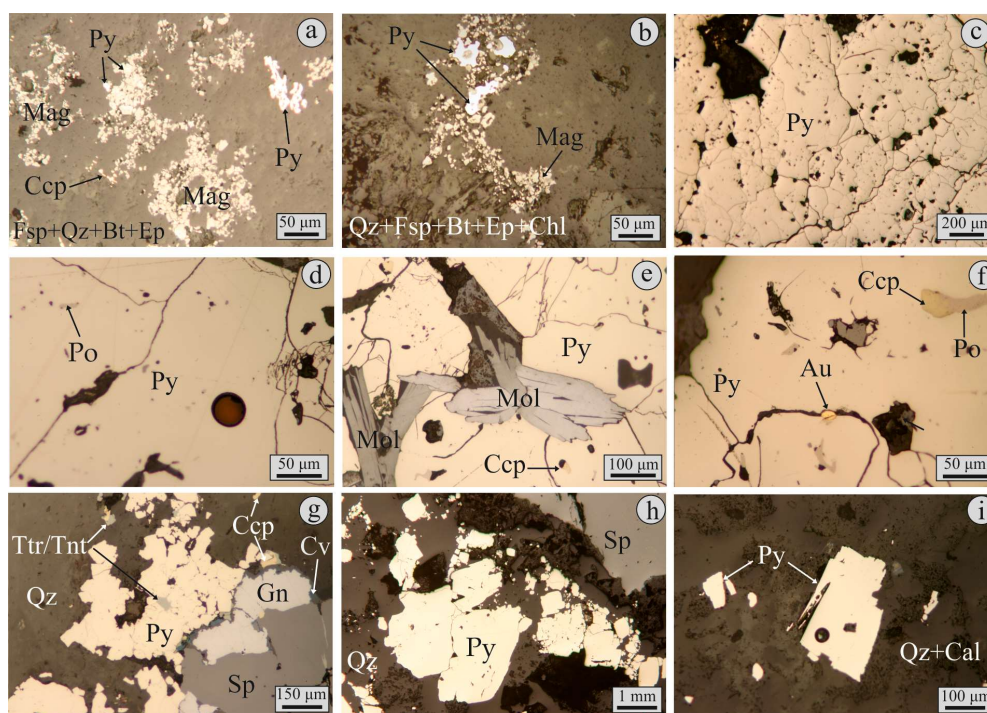


**Figure 7.** Reflected light photomicrographs of pyrite and associated opaque minerals from different mineralization events in the Pagoni Rachi prospect. (a) Fine grained magnetite (Mag) in association with pyrite (Py) and chalcopyrite (Ccp), in calcic/potassic matrix dominated by feldspar (Fsp, orthoclase, and/or albite), quartz (Qz), feldspar (Fsp, orthoclase, and/or albite) biotite (Bt) and epidote (Ep), M-type vein (sample KMPR74); (b) Magnetite (Mag) along with pyrite (Py) in sodic/potassic-calcic altered granodiorite porphyry, consisting of quartz (Qz), feldspar (Fsp, albite, and/or orthoclase), biotite (Bt), epidote (Ep), and chlorite (Chl), M-type vein, (sample KMPR68); (c,d) Massive, subhedral to anhedral pyrite (Py), including minor pyrrhotite (Po), D-type vein, (sample KMPR66). Note in (d) the black circle indicates the laser-ablation ICP-MS analysis spot; (e) Subhedral pyrite (Py) intergrown with molybdenite (Mol) and including minor chalcopyrite (Ccp), D-type vein (sample KMPR66); (f) Native gold (Au) associated with pyrite (Py), which includes pyrrhotite (Po) and chalcopyrite (Ccp), D-type vein (sample KMPR66); (g) Euhedral pyrite (Py) in association with galena (Gn), sphalerite (Sp), covellite (Cv), and fahlores (Ttr/Tnt), in quartz (Qz), E-type vein (sample KMPR53); (h) Coarse-grained, euhedral pyrite (Py) and sphalerite (Sp) in quartz (Qz), epithermal-style vein (sample KMPR53); (i) Pyrite grain included in a quartz (Qz) and calcite (Cal) dominated matrix. The black circle marks the laser-ablation ICP-MS analysis spot, E-type vein (sample KMPR53).

Base and precious metal-bearing, epithermal-style veins (E-type) occur laterally and/or crosscut the porphyry-style mineralization. They are composed mainly of alternating bands of quartz and calcite (Figure 6h,i). In these veins, pyrite forms medium- to coarse-grained (up to 1 cm) crystals that occur either as isolated grains in the quartz and calcite-dominated matrix, or as aggregates with other sulfides. They exhibit idiomorphic, commonly cubic, shapes (Figures 7g–i and 8f). Pyrite in E-type veins is associated with galena, sphalerite, chalcopyrite, covellite, and tetrahedrite-tennantite group minerals (Figure 7g–i). The other sulfides as well as the fahlores, develop as rims on or as inclusions in pyrite crystals, or in fractures, which suggests they postdated the formation of pyrite.

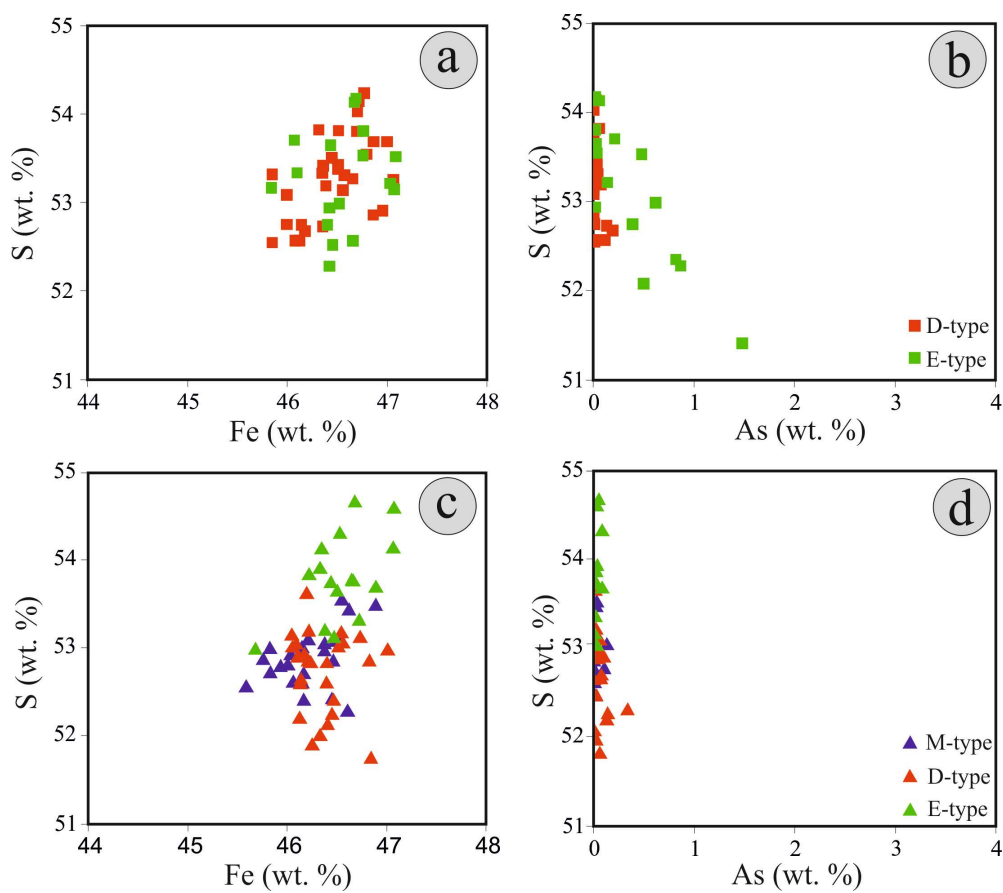


**Figure 8.** Concentration of S versus Fe and As (in wt.%) in pyrite from different mineralization events at the Konos Hill ((a,b), respectively) and the Pagoni Rachi ((c,d), respectively) porphyry-epithermal prospects.

#### 4.2. Major and Trace Element Geochemistry of Pyrite

Electron probe micro-analyses (EPMA) of various generations of pyrite are summarized in Table 2 and plotted in Figure 8. Results of the LA-ICP-MS analyses of pyrite from the Konos Hill and the Pagoni Rachi prospect are shown in Tables 3 and 4, respectively. Chemical differences between the various generations of pyrite from both prospects, based on their trace element content, are illustrated in Figures 9 and 10.

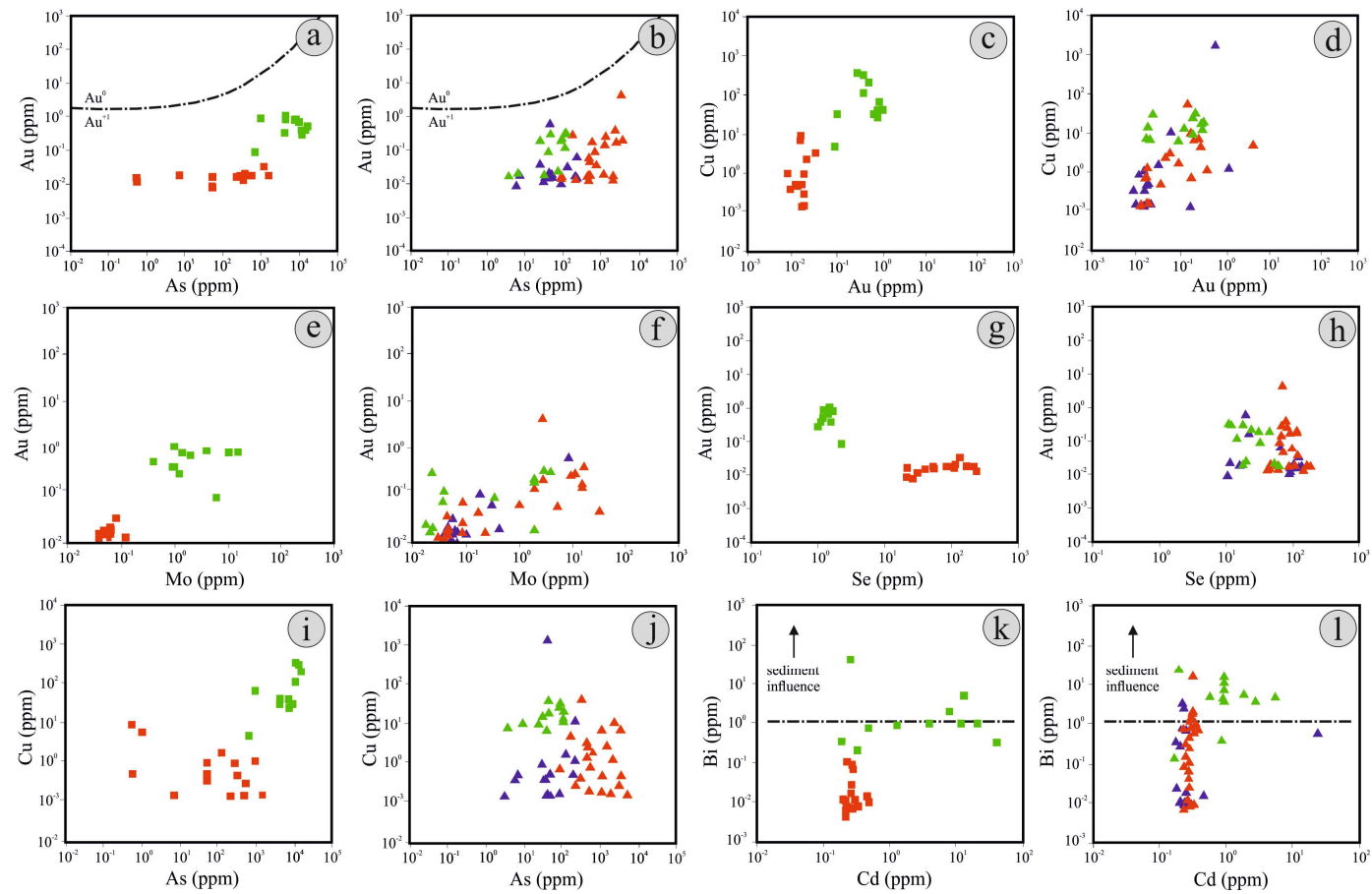
**Table 2.** EPM analyses of various pyrite generations from the Konos Hill and Pagoni Rachi porphyry/epithermal prospects. All values are reported in wt.%. For the full dataset please refer to supplementary Table S2.

Konos Hill Prospect												
Type	D-type ( <i>n</i> = 29)				E-type ( <i>n</i> = 17)							
Element	MIN	MAX	SD	AVRG	MIN	MAX	SD	AVRG				
As	0.04	0.19	0.04	0.03	0.11	1.48	0.41	0.32				
Fe	45.85	47.06	0.34	46.47	45.84	48.37	0.58	46.70				
Cu	b.d.l.	0.05	0.01	0.01	b.d.l.	0.23	0.06	0.04				
Ni	b.d.l.	b.d.l.	-	-	b.d.l.	b.d.l.	-	-				
Co	0.05	0.14	0.02	0.08	b.d.l.	0.03	0.03	0.02				
Au	b.d.l.	0.08	0.03	0.02	b.d.l.	0.07	0.01	0.00				
Se	b.d.l.	0.06	-	-	b.d.l.	b.d.l.	-	-				
S	52.55	54.24	0.48	53.29	51.41	54.18	0.74	53.14				
Total	98.56	101.13	0.71	99.91	99.58	100.77	0.58	100.17				

Pagoni Rachi Prospect												
Type	M-type ( <i>n</i> = 22)				D-type ( <i>n</i> = 26)				E-type ( <i>n</i> = 15)			
Element	MIN	MAX	SD	AVRG	MIN	MAX	SD	AVRG	MIN	MAX	SD	AVRG
As	b.d.l.	0.14	0.03	0.02	b.d.l.	0.34	0.07	0.05	b.d.l.	0.09	0.03	0.02
Fe	45.59	46.89	0.32	46.23	46.05	47.01	0.26	46.35	45.68	47.07	0.34	46.54
Cu	b.d.l.	0.05	0.02	0.01	b.d.l.	0.04	0.01	0.01	b.d.l.	0.05	0.02	0.01
Ni	b.d.l.	0.03	0.01	0.00	b.d.l.	0.20	0.04	0.01	b.d.l.	b.d.l.	-	-
Co	0.05	0.64	0.14	0.13	0.08	0.30	0.06	0.07	b.d.l.	0.01	-	-
Au	b.d.l.	0.16	0.04	0.02	b.d.l.	0.16	0.04	0.04	b.d.l.	0.06	-	-
Se	b.d.l.	b.d.l.	-	-	b.d.l.	0.10	0.02	0.04	b.d.l.	b.d.l.	-	-
S	52.27	53.70	0.35	52.88	51.74	53.61	0.45	52.73	52.98	54.66	0.49	53.79
Total	98.69	100.55	0.53	99.29	98.73	100.23	0.49	99.26	98.70	101.31	0.75	100.09

(*n* = number of analyses; MIN = minimum value; MAX = maximum value; SD = standard deviation; AVRG = average value; b.d.l. = below detection limit).



**Figure 9.** Trace elements variation plots of pyrite from different mineralization events at the Konos Hill (a,c,e,g,i,k) and the Pagoni Rachi (b,d,f,h,j,l) porphyry-epithermal prospects (same symbols as in Figure 8; values in ppm). (a,b) As versus Au. The black, dash-dotted curve represents the solubility limit of Au as a function of As concentration [8]; (c,d) Au versus Cu; (e,f) Mo versus Au; (g,h) Se versus Au; (i,j) As versus Cu; (k,l) Bi versus Cd, adopted from Keith et al. [7]. The maximum Bi value of 7451 ppm, attributed to Bi-bearing inclusion, has been excluded from the plot in 9l.

**Table 3.** LA-ICP-MS analyses of various pyrite generations from the Konos Hill porphyry/epithermal prospect. All values are reported in ppm. For the full dataset please refer to supplementary Table S3.

Element	D-type (n = 15)				E-type (n = 12)			
	MIN	MAX	SD	AVRG	MIN	MAX	SD	AVRG
Mn	0.57	1.12	0.19	0.75	0.42	13	4.90	6.55
Co	0.56	1395	378	254	0.30	457	156	101
Ni	3.50	46	15	18	1.96	628	196	102
Cu	0.30	9.12	2.99	2.33	4.78	351	124	111
Zn	2.11	3.35	0.47	2.75	3.99	49	15	18
Ga	0.13	0.56	0.25	0.27	0.17	2.00	0.53	0.85
Ge	1.03	1.22	0.09	1.15	0.75	2.20	0.52	1.29
As	7.22	1577	485	436	688	16,429	5207	8203
Se	21	233	69	93	b.d.l	b.d.l.	-	-
Mo	0.12	0.12	-	0.12	0.41	15	4.85	4.00
Ag	b.d.l.	b.d.l.	-	-	0.92	19	6.38	8.76
Cd	0.47	0.50	0.02	0.49	0.49	41	13	13
In	b.d.l.	b.d.l.	-	-	0.04	0.25	0.08	0.09
Sn	0.16	0.21	0.04	0.19	0.29	9	3.18	1.81
Sb	0.10	0.11	0.01	0.10	1.98	292	99	131
W	0.04	0.04	-	0.04	0.01	0.40	0.13	0.18
Au	0.02	0.06	0.01	0.03	0.09	1.10	0.30	0.62
Tl	0.00	0.01	0.00	0.01	0.05	18	6.31	11
Pb	0.05	0.48	0.13	0.27	34	898	277	401
Bi	0.02	0.11	0.04	0.06	0.21	42	12	4.55

n = number of analyses; MIN = minimum value; MAX = maximum value; SD = standard deviation; AVRG = average value; b.d.l. = below detection limit.

**Table 4.** LA-ICP-MS analyses of various pyrite generations from the Pagoni Rachi porphyry/epithermal prospect. All values are reported in ppm. For the full dataset please refer to supplementary Table S3.

Element	M-type (n = 16)				D-type (n = 22)				E-type (n = 12)			
	MIN	MAX	SD	AVRG	MIN	MAX	SD	AVRG	MIN	MAX	SD	AVRG
Mn	0.53	9.10	2.64	2.74	0.59	5.83	1.35	1.87	0.92	264	80	58
Co	0.49	13	3.63	3.67	0.28	576	169	97	1.24	198	49	55
Ni	2.88	77	22	20	3.27	113	25	22	4.38	52	17	28
Cu	0.54	1659	524	168	0.49	9824	2530	678	6.22	31	8.52	16
Zn	2.04	2751	734	199	3.02	3.55	0.22	3.39	3	2012	669	326
Ga	0.15	0.16	0.01	0.15	0.12	0.70	0.26	0.37	1	4	1.25	2.37
Ge	1.09	1.22	0.07	1.16	1.09	1.59	0.18	1.27	1.1	3	0.65	1.64
As	3.20	233	80	78	91	3745	1084	1166	3.77	121	43	63
Se	11	137	45	77	42	187	39	91	11	63	17	29
Mo	0.11	8.69	4.20	2.39	0.09	33	9.98	11	0.36	4	1.22	2.23
Ag	b.d.l.	2.10	-	2.10	0.56	0.56	-	0.56	0.56	2	0.49	1.32
Cd	b.d.l.	27	18	14	b.d.l.	b.d.l.	-	-	0.61	6	1.65	1.75
In	b.d.l.	0.20	0.10	0.09	0.03	0.04	0.01	0.03	0.09	0.10	0.01	0.10
Sn	b.d.l.	0.17	-	0.17	0.13	0.19	0.04	0.16	b.d.l.	0.20	0.03	0.18
Sb	0.07	1.08	0.44	0.50	0.13	0.57	0.20	0.33	0.17	1.77	0.46	0.53
W	b.d.l.	0.24	-	0.24	0.03	0.23	0.09	0.08	0.01	0.11	0.04	0.06
Au	0.02	0.61	0.25	0.18	0.04	4.35	1.21	0.52	0.09	0.33	0.09	0.22
Tl	0.01	0.02	0.00	0.01	0.01	0.01	-	-	0.06	0.21	0.05	0.15
Pb	0.04	129	43	24	0.05	18	5.09	3.43	34	620	166	134
Bi	0.02	4.85	1.76	1.07	0.03	18	4.06	3.04	0.14	7451	628	2148

n = number of analyses; MIN = minimum value; MAX = maximum value; SD = standard deviation; AVRG = average value; b.d.l. = below detection limit.

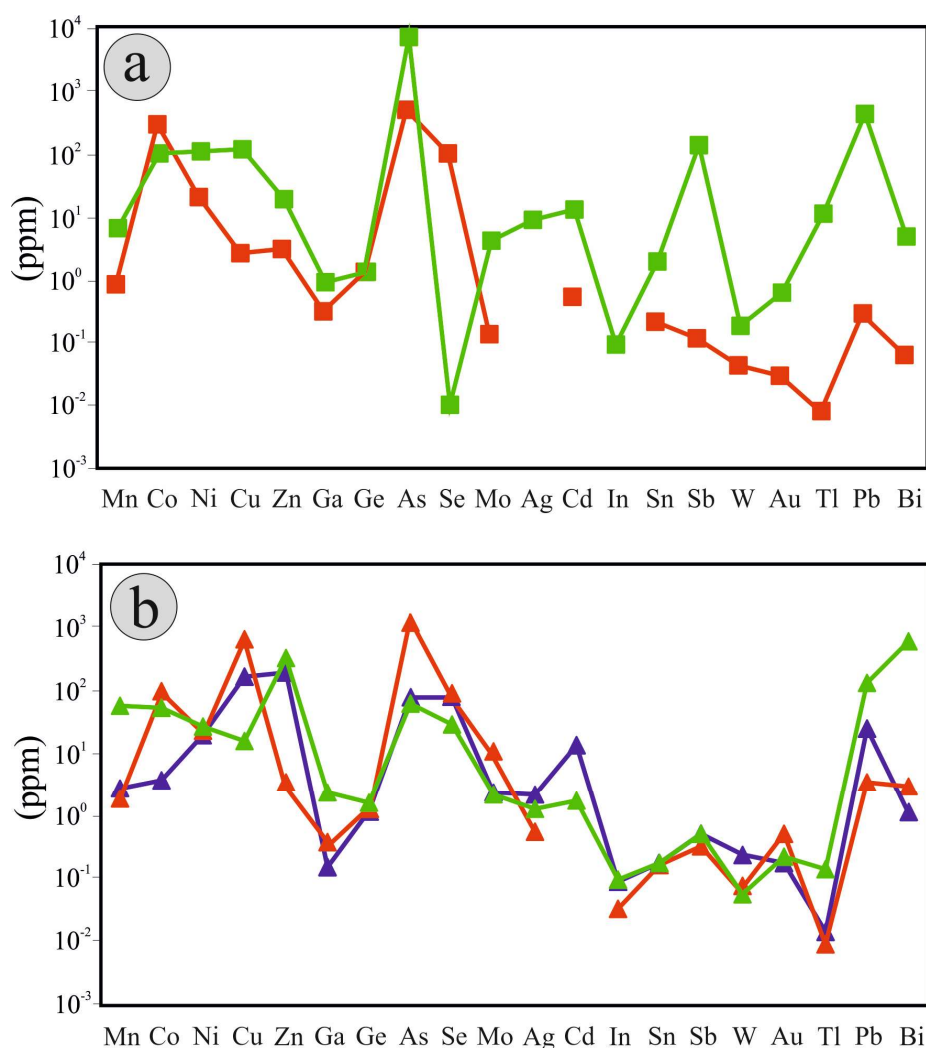


**Figure 10.** Multi-element variation plots (based on average values for each element) of pyrite from different vein types at the Konos Hill (a) and the Pagoni Rachi (b) porphyry-epithermal prospects (symbols as in Figure 8; values in ppm).

#### 4.2.1. EPM Analyses

The Fe and S content of pyrite from the Konos Hill prospect varies in the two mineralization stages (Table 2). Specifically, the Fe content of pyrite from the D-type veins ranges between 45.85 and 47.06 wt.%, while the S content is in the range between 52.55 and 54.24 wt.%. In E-type veins, the compositional variation is wider for both elements: Fe ranges between 45.84 and 48.37 wt.%, and, between 51.41 and 54.18 wt.% (Figure 8a). These variations partly reflect the presence of trace element impurities that substitute for both Fe and S, in the structure of pyrite [4,6,79]. Arsenic in pyrite from D-type veins is minor, reaching values of up to 0.19 wt.% and thus, it does not display any systematic relation to the content of sulfur. However, in E-type veins, As is a major impurity and reaches values of up to 1.48 wt.%. The negative correlation between the two elements indicates substitution of S by As (Figure 8b).

In the Pagoni Rachi prospect, pyrite from the early, magnetite-rich (M-type) veins is characterized by Fe and S values that are relatively homogenous and range from 45.59 to 46.89 wt.% and 52.27 and 53.70 wt.%, respectively (Figure 8c). Compared to pyrite from these veins, pyrite from the D-type veins is characterized by slightly higher Fe values, that are in the range 46.05–47.01 wt.%, and by slightly lower S values, that vary from 51.74 to 53.61 wt.%. The higher values for both elements, are in pyrite from the E-type veins. In these grains of pyrite, Fe ranges between 45.68 wt. and 47.07 wt.%, and S

between 52.98 and 54.66 wt.% (Figure 8c). Arsenic is within the range of trace concentrations of up to 0.14 wt.%, 0.34 wt.%, and 0.09 wt.%, that is observed in pyrite from the M-, D-, and E-type veins, respectively (Figure 8d). The majority of the other elements are mostly below detection limits (Table 2).

#### 4.2.2. LA-ICP-MS Analyses

The trace elements concentration of pyrite exhibits important variations between the two stages of mineralization at the Konos Hill prospect (Table 3). The most abundant trace element is As, which reaches values up to 1577 ppm in pyrite from D-type veins, and up to 16,429 ppm in pyrite from E-type veins. Pyrite from both stages is characterized by relatively low Au content, which contains values of only up to 0.06 ppm and 1.10 ppm, respectively. The Ag content reflects a preferable enrichment in the late stage of the mineralization (up to 19 ppm in E-type veins), relative to D-type veins where its concentration never exceeds the detection limit. Regarding the rest of the trace elements, pyrite from the D-type veins is depleted in all elements except for Co (up to 1395 ppm) and Se (up to 233 ppm) in contrast to pyrite from E-type veins, which is characterized by much less Co (up to 457 ppm) and is depleted in Se (below the detection limit). Nickel and Cd have an opposite behavior to Co, being enriched in pyrite from E-type veins (up to 628 ppm and 41 ppm, respectively), relative to pyrite from D-type veins (up to 46 ppm and 0.50 ppm, respectively). Other notable concentrations in pyrite from E-type veins that are generally well above detection limits are Pb (up to 898 ppm), Cu (351 ppm), Sb (up to 292 ppm), and Bi (up to 42 ppm). Molybdenum is characterized by very low concentrations in D-type pyrite but reaches values of up to 15 ppm in pyrite from the late, E-type veins. Traces of Ga and Ge occur in both D- and E-type pyrite, however, the average values for both elements are higher in the epithermal stage with average values for Ga and Ge are 0.27 ppm and 1.15 ppm at the Konos Hill prospect.

In the Pagoni Rachi prospect, LA-ICP-MS analyses reveal a large variation in the concentration of trace elements among the various generations of pyrite (Table 4). Pyrite from the early magnetite veins (M-type) is characterized by very low contents of Au and Ag (up to 0.61 ppm and 2 ppm, respectively), and elevated concentrations of Zn and Cu, which reach values of up to 2751 ppm and 1659 ppm, respectively. The concentration of As content is relatively low (maximum value is 233 ppm), but it is relatively enriched in Se (up to 137 ppm) and Pb (up to 129 ppm). Other elements that exhibit low concentrations are Ni (up to 77 ppm), Cd (up to 27 ppm), Co (up to 13 ppm), and Mo (up to 9 ppm), while the rest of the elements analyzed are generally below 5 ppm.

Pyrite in D-type veins is enriched in Cu (up to 9824 ppm), while the concentration of As varies between 91 and 3745 ppm. Cobalt, Se, and Ni display relatively high concentrations of up to 576 ppm, 187 ppm, and 113 ppm, respectively. Molybdenum is as high as 33 ppm, while Au and Ag reach concentrations of up to 4 ppm and 0.6 ppm, respectively. The rest of the elements are characterized by very low concentrations (generally below 5 ppm) except for Pb and Bi, both of which reach values of up to 18 ppm.

Pyrite in E-type veins contains Bi and Zn with up to 7451 ppm and 2012 ppm, respectively, with the latter being comparable to the Zn content of in pyrite in M-type veins. Other elements that are enriched in pyrite from E-type veins include Pb (up to 620 ppm), Co (up to 198 ppm), As (up to 121 ppm), and Se (11–63 ppm). Copper (up to 31 ppm) is depleted in pyrite in E-type veins compared to that in earlier stages of metallic mineralization. Moreover, the concentration of Au is relatively small (up to 0.33 ppm), while Ag, which also displays small concentration is preferably found in pyrite from the E-type veins (up to 2 ppm). Additionally, minor amounts of Ga and Ge were measured, with average values (2.37 ppm and 1.64 ppm, respectively) being higher compared to those in pyrite from M- and D-veins (Table 4).

## 5. Discussion

### 5.1. Distribution of Trace Elements in Porphyry-Style Pyrite

Pyrite from the early stages of porphyry-style deposits is commonly characterized by a poor budget of trace elements (e.g., [6,19,30]).

The gold content of pyrite in the Konos Hill and the Pagoni Rachi systems is relatively low. The only exception is pyrite from the D-type veins in the Pagoni Rachi prospect, where Au values reach up to 4.35 ppm. This is consistent with the findings of Voudouris et al. [65], who reported that the major introduction of gold in the system occurred during the D-event. Since the speciation of gold in pyrite is highly dependent on its arsenic content [8], it is evident from the plots in Figure 9a,b that the gold concentration of pyrite from Konos Hill and Pagoni Rachi never exceeds the solubility limit of Au as a function of As. Thus, no gold nanoparticles ( $\text{Au}^0$ ) are present, meaning that gold is incorporated as a non-stoichiometric substitution in the structure of pyrite ( $\text{Au}^{+1}$ ). However, a visual correlation between Au and As is evident (Figure 9a,b). Regarding its relation to Cu, Au displays a weak correlation in pyrite from all stages at the Pagoni Rachi system (Figure 9c,d).

Given the absence of an early M-type event in the Konos Hill prospect, the hypothesis of the deficiency of pyrite in trace elements during the early stages of the porphyry mineralization can only be tested for the Pagoni Rachi prospect, where magnetite-veins constitute the first ore stage [65,66]. Pyrite from M-type veins is generally characterized by small concentrations of trace elements, but there are a few exceptions; a high concentration of Cu, Zn, and Se and minor Cd is evident. The values that characterize the majority of these elements are higher in the Pagoni Rachi prospect compared to those described from mineralization related to sodic-potassic and potassic alteration in other deposits, for example, the Pebble porphyry Cu-Mo-Au deposit [31]. The abundance of chalcopyrite in association with pyrite and magnetite in M-veins suggests elevated availability of Cu during this event, and probably indicates the presence of  $\text{Cu}^{2+}$  in solid solution in pyrite. A similar abundance in the precipitating fluid can be inferred for Zn, as it also shows elevated values.

These findings from M-type related pyrite are consistent with the of Mavrogenatos et al. [66], who described elevated content of Cu and Zn in hydrothermal magnetite, at the Pagoni Rachi prospect, thus strengthening the hypothesis of elevated concentrations of Cu and Zn in the precipitating fluid. Given the highly-saline nature of the fluid that precipitated A-type quartz veins, which formed synchronously with M-type veins (38.9–69.9 wt.% NaCl equivalent [65]), the Zn (and possibly Cu) enrichment in the brine during this stage is further supported by the work of Ding and Seyfried [80], Bazarkina et al. [81], and Pokrovski et al. [82], who suggested that metals with a chloride affinity like Zn, are fixed in dense, highly saline brines.

The Mo values of pyrite from the porphyry stages at both prospects are low (up to 15 ppm at Konos Hill and up to 10 ppm at Pagoni Rachi), although molybdenite is widespread in the porphyry-style mineralization (Figure 9e,f). This suggests that Mo is preferably precipitating as a metal sulfide rather than substituting in the structure of pyrite. The correlation between Mo and Au in pyrite from the D-type veins at Pagoni Rachi (Figure 9f) is strong evidence of the contemporaneous introduction of these elements during this mineralization stage. A similar hypothesis can be made for Au with Ag, and Mo in the early magnetite veins.

High concentration of selenium in D-type pyrite from both prospects as well as in pyrite from M-type veins at the Pagoni Rachi prospect is notable. According to Huston et al. [13] and Layton-Matthews et al. [83], who conducted thermodynamic modelling on the chemistry of selenium, the Se content of pyrite is solely a function of the  $\Sigma\text{Se}/\text{S}$  ratio of the precipitating fluid, and thus it reflects its availability in the precipitating hydrothermal fluids. There is no systematic relationship between Se and the Au content of pyrite in the deposits studied here (Figure 9g,h). The correlation of Se with other trace elements, like Co and/or Ni (in some porphyry and the epithermal stages of the studied prospects), could reflect the presence of selenides that incorporate such elements (e.g., like the mineral tyrellite  $[\text{Cu}(\text{Co},\text{Ni})_2\text{Se}_4]$ , [10]). This speculation is in agreement with the findings

of Voudouris et al. [65], who reported the presence of two unnamed, Se-bearing inclusions in pyrite. However, the obtained ablation patterns do not clearly show the presence of such inclusions and suggests a homogeneous distribution of these elements in pyrite.

### 5.2. Distribution of Trace Elements in Epithermal-Style Pyrite

The compositional variation between pyrite from the M-, D-, and E-type veins (Figure 10) is most likely due to variation in the composition of the precipitating fluid. For example, this can result from the mixing between different pulses of hydrothermal fluids, a common and repeated process during the evolution of porphyry systems (e.g., [29,84–89]). However, a roughly common trend is present for the metal endowment of the two studied systems (Figure 10).

Voudouris et al. [65] stated that the base and precious metal bearing veins (E-type) may represent the root zones of high-sulfidation veins at higher topographic levels of a given ore system, which seems to be the case for the higher levels of the Konos Hill prospect, where advanced argillic alteration assemblages occur in association with (mostly oxidized) high-sulfidation mineralization [49,61,62]. However, it remains speculative whether such a lithocap once overprinted the Pagoni Rachi system. Mineralogical similarities between D- and E-type veins (e.g., the presence of molybdenite or tellurides [65]) record the transition from the porphyry to the epithermal environment and is reflected in the changes in the trace element content of pyrite.

As indicated by their low visual correlation, As and Cu appear to have been decoupled (Figure 9i,j) in the porphyry-style stages of mineralization in the Konos Hill and the Pagoni Rachi prospects. This is in accordance with the findings of Reich et al. [6] who studied the trace elements distribution in pyrite from the Dexing porphyry Cu-Mo-Au deposit (China) and demonstrated that Cu is geochemically decoupled from As. This further suggests that this selective partitioning of metals into pyrite probably reflects compositional variations in the hydrothermal fluid [6]. The presence of micrometer-scaled chalcopyrite inclusions in D-type veins from the Pagoni Rachi prospect, likely indicates Cu-saturated conditions derived from cooling of high-temperature pyrite forming fluids as the hydrothermal system evolved with time [78]. Chalcopyrite inclusions in pyrite from D-type veins at Pagoni Rachi are indicated by the LA-ICP-MS profile (Figure 11a) where, a spot analysis yielded a remarkably high value (9824 ppm) of Cu.

This decoupling behavior does not characterize pyrite from E-type veins, indicating a more homogeneous introduction of Cu and As, at the epithermal stages (E-type veins) of both prospects. Regardless, the As content of pyrite from the epithermal stage of both prospects is relatively low, when compared to other epithermal gold deposits (e.g., Yanacocha, Peru, [29]), thus indicating a restricted activity of As in the late hydrothermal fluids [19] and/or its preferable incorporation into other As-bearing phases (e.g., fahlores).

Another distinctive feature of pyrite from the late E-type veins, is their Pb content. Generally, Pb displays high concentrations in the epithermal-style veins (up to 898 ppm and 620 ppm at Konos Hill and Pagoni Rachi, respectively) rather than in the porphyry mineralization. These values are likely due to Pb substituting for Fe in the structure of pyrite, despite the much larger size of the Pb ion, as indicated by the flat LA-ICP-MS Pb-patterns (Figure 11).

The transition between the porphyry and epithermal stages is also supported by the presence of Se in pyrite throughout the depositional history of both systems, thus indicating that Se was present during the evolution of the porphyry to epithermal stages.

A distinctive feature of pyrite from the E-type stage in the Konos Hill and Pagoni Rachi prospects (Figure 9k,l) is their Bi content, compared to pyrite from the other stages of mineralization. The majority of the analytical spots yielded values >1 ppm Bi, similar to other epithermal pyrite elsewhere, while the extreme Bi value of 7451 ppm, indicates the presence of a Bi-bearing phase during the ablation procedure, as reflected by the peak for Bi in Figure 11b. The presence of Bi along with Te and Au in the mineralization, in the form of Bi-tellurides/sulfosalts or Bi-bearing galena, appears to be diagnostic of the proximity to a magmatic center [55,90]. This characteristic holds true for both the Konos Hill

and the Pagoni Rachi epithermal style veins, as they occur laterally or overprint the porphyry-stage mineralization. Thus, Bi which was likely transported by magmatic volatiles that was derived from the causative intrusion into the hydrothermal fluids, could have been incorporated into the structure of pyrite as well as forming Bi sulfosalts and tellurides in E-type veins [65].

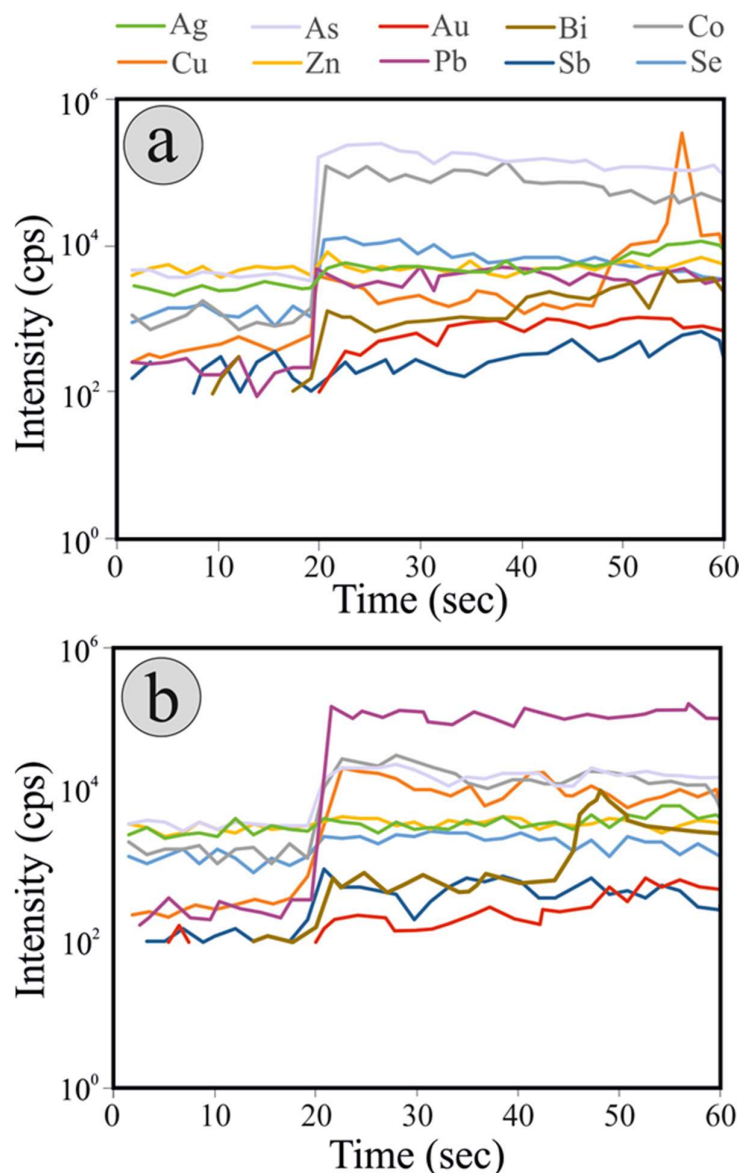


**Figure 11.** Time-resolved laser ablation ICP-MS depth profiles of Ag, As, Au, Bi, Co, Cu, Zn, Pb, Sb, and Se in pyrite. (a) D-type vein, (sample KMPR66). Most of the elements are characterized by homogeneous distribution, as expressed by their flat concentration patterns. The spiky pattern of Cu indicates the presence of submicroscopic inclusions (chalcopyrite); (b) E-type vein, (sample KMPR53). All elements but Bi show homogeneous distribution in pyrite. The spiky pattern of Bi is indicative of the presence of a submicroscopic, Bi-bearing phase (bismuthinite?).

### 5.3. Fingerprinting the Transition from the Porphyry to Epithermal Environment—Comparison to Other Porphyry/Epithermal Systems

The composition of pyrite is known to roughly reflect the metal endowment of the precipitating fluid in many hydrothermal systems, with the porphyry-epithermal association being, among others, a prominent example [3]). Despite the relatively restricted availability of compositional data for pyrite

from porphyry systems worldwide, the chemical composition of pyrite from the Konos Hill and the Pagoni Rachi porphyry/epithermal systems seems to follow the general trend of other deposits, although there are notable differences.

The gold content of pyrite in the porphyry mineralization studied here is generally in the range of values that commonly characterize pyrite from porphyry-style deposits, which is characterized by low values and a homogeneous distribution. As indicated by the gold concentration in pyrite as a function of its As content (Figure 9a,b), the pyrite precipitating fluids at both deposits remained undersaturated in Au (cf. [6]). At the Konos Hill prospect, the gold content of pyrite increases from D-type veins to E-type veins (average values from 0.03 ppm to 0.62 ppm respectively), in accordance with an increase in the As content. Similar behavior has been described from other porphyry/epithermal deposits and prospects, like the Agua Rica porphyry/high sulfidation deposit [19] and the Lienetz porphyry-related epithermal system [20]). This observation has been attributed to the preferable scavenging of Au by the hydrothermal fluid in the high-temperature porphyry environment, in contrast to the shallow epithermal conditions, which favors the precipitation of gold. This accounts for the much higher Au grades in the epithermal deposits [3,7]. However, at the Pagoni Rachi system, early pyrite from M-type veins, as well as late pyrite from the epithermal stage, is characterized by gold contents (mean values of 0.18 ppm and 0.22 ppm, respectively), which are lower compared to pyrite from D-type veins (average 0.52 ppm Au). The As content follows the same trend: the maximum As values correlate with gold and are higher in pyrite in D-type veins. The late-stage epithermal pyrite is characterized by considerable lower As (and Au) content, which contrasts to that observed in other analogous porphyry/epithermal systems, where the transition from the porphyry to the epithermal environment is marked by an increase in the Au and As content of pyrite (e.g., [6]).

Another distinctive feature of early, porphyry-style pyrite worldwide, is their enrichment in Co, Se, Ni, and Cu [6,20,31]. Early M-vein hosted pyrite in the Pagoni Rachi system supports this observation. In the case of Pagoni Rachi the enrichment in Co, Se and Cu, is higher in pyrite D-type veins. This feature also characterizes pyrite in D-type veins in the Konos Hill system. The relative enrichment is apparent in Figure 12a, where, compared to pyrite in other porphyry-style deposits, pyrite from the prospects studied here displays higher Se concentrations. With regards to the Ni content of pyrite in the Konos Hill prospect, it is preferably enriched in late, E-type pyrite (average value 102 ppm), in contrast to other deposits, where Ni is usually enriched in pyrite in early, porphyry-style mineralization (e.g., [19,20,33]). The lack of enrichment in the Ni content of pyrite is present in the Pagoni Rachi system.

Recently, Alford et al. [33] proposed that a positive correlation between the Cu/Ni and Au/Co ratios occurs in pyrite formed during the transition from the porphyry to the epithermal style in the Lienetz mineralization in the Lihir deposit (Papua New Guinea). This correlation also holds true for pyrite studied here, owing mostly to the high Co values in pyrite and their generally low Au contents in porphyry-style mineralization (Figure 12b). This is more apparent for the ratios obtained from pyrite in the Konos Hill deposit. Although the same observation generally holds for correlation between Cu/Ni and Au/Co ratios for pyrite in the Pagoni Rachi prospect, the high Au content of pyrite from the D-type veins, as well as the higher concentration of Cu in pyrite in M- and D-vein pyrite, leads to an overlap with pyrite from the late, epithermal stage. These similarities imply, that late-stage mineralization that formed from hydrothermal fluids associated with the Pagoni Rachi record an evolution of a genetically-linked parental magmatic fluid, and its subsequent mixing with non-magmatic fluids, which lead to the formation of the epithermal-style mineralization. This is further supported by fluid inclusion studies of Voudouris et al. [65], who suggested that the formation of porphyry/epithermal mineralization at Pagoni Rachi was the result of the evolution of a hydrothermal fluid under constantly decreasing pressure and temperature conditions.

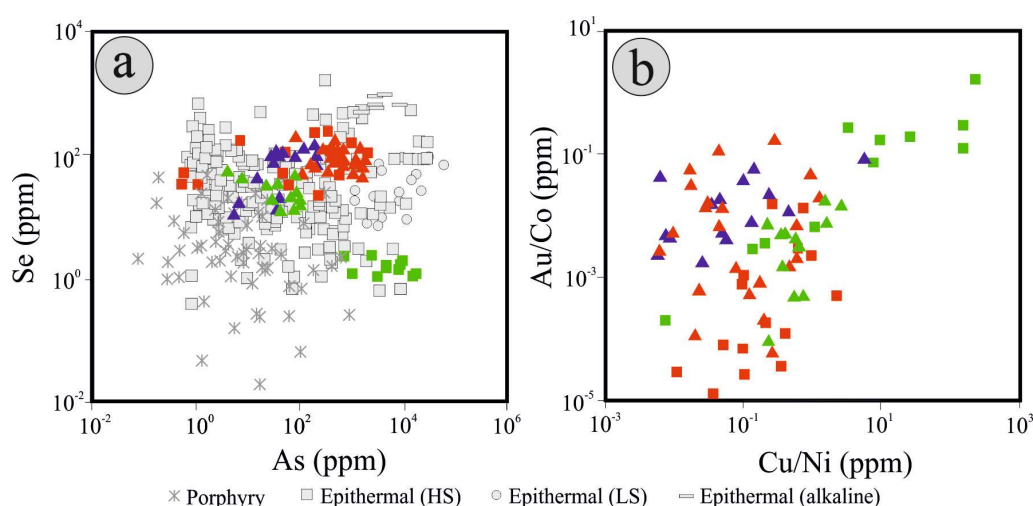


**Figure 12.** (a) Variation of As versus Se in pyrite from the present study compared to pyrites from orogenic Au, Carlin-type, high-sulfidation (HS) epithermal, low-sulfidation (LS) epithermal, alkaline rock-hosted epithermal and porphyry Cu deposits (grey symbols). Adopted from Keith et al. [10]; (b) Cu/Ni versus Au/Co plot for various pyrite generations from the studied porphyry/epithermal prospects (adopted from Alford et al. [33]). Symbols as in Figure 8.

Several trace elements (including Pb, Sb, Bi, Ag) are concentrated in late E-type pyrite in the Konos Hill and Pagoni Rachi prospects, compared to their porphyry-style counterparts. An analogous observation by Franchini et al. [19] to propose that enrichment in this chalcophile group of trace elements in the epithermal pyrite in the Agua Rica deposit could partly be the result of leaching and remobilization from earlier (porphyry-style) pyrite. This hypothesis could be true for the prospects studied here and could be the mechanism that contributed (at least partly) to the metal budget of the epithermal-style pyrite. This is especially the case for the Pagoni Rachi prospect where, the presence of Se in late-stage (epithermal) pyrite supports the concept that the deep porphyry system gradually evolved to shallower epithermal conditions.

Based on the studies of Voudouris et al. [55,65,90], the Konos Hill and the Pagoni Rachi porphyry-epithermal prospects contain a variety of minerals that reflect the trace elements that are also enriched in pyrite (e.g., Au, Bi, Se). Their presence adds a new perspective to the economic significance of these deposits. The current study complements recent studies by Voudouris et al. [55,90,91], Voudouris [92], Melfos and Voudouris [93], and Mavrogonatos et al. [66] that identified potential mineralogical vectors useful in the exploration for precious and critical metals in porphyry/epithermal systems in Greece.

The LA-ICP-MS studies here reveal that gold is incorporated into the structure of pyrite rather than occurring as nano-, or micro- inclusions. Furthermore, the high correlation between Au and Cu in pyrite from M-type veins, and the high Se content of pyrite in D-type veins in both prospects, could be evaluated as an exploration tool for Au in other porphyry-epithermal prospects in northern Greece (particularly the province of Thrace).

## 6. Conclusions

Pyrite in the Konos Hill and Pagoni Rachi porphyry-epithermal prospects in NE Greece displays important variations in texture and trace element content in the various mineralization stages. Porphyry-style pyrite from both prospects is commonly fine-grained and anhedral and is associated mainly with varying amounts of magnetite, chalcopyrite, molybdenite, bornite, pyrrhotite, and native gold. In contrast, pyrite from the late epithermal (E-type) veins form idiomorphic, (commonly cubic) medium- to coarse-grained crystals that are associated with chalcopyrite, sphalerite, galena, and tetrahedrite-tennantite group minerals.

At the Konos Hill prospect, D-type veins associated with sericitic altered granodiorite, pyrite is characterized by elevated concentrations of Se, Cu, Co, and minor Zn, but is depleted in other trace elements. Pyrite in late, epithermal-style (E-type) calcite-quartz veins, associated with argillic alteration, is enriched in As, Cu, Pb, Ni, Sb, Bi, and minor Ag. In contrast, pyrite in M-type veins in the Pagoni Rachi prospect is associated with sodic/potassic-calcic alteration that is enriched in Cu, Zn, Se and minor Cd, but depleted in other trace elements, as commonly the case for early stages of porphyry-style mineralization elsewhere. The D-type veins host Au-rich pyrite that is also characterized by high concentrations of Cu (partly attributed to nano-inclusions), Co, and Se. In late E-type veins, pyrite is characterized by the abundance of Bi (also present as submicroscopic inclusions), Pb and Zn, with minor amounts of Se, and traces of Ga and Ge.

The presence of gold as a non-stoichiometric substituting element in the structure of pyrite and not as nanoparticles is a common feature for both prospects, regardless of the stage of metallic mineralization. Gold correlates with the As content of pyrite, especially in D-type veins from the Pagoni Rachi prospect, in contrast to many other porphyry-epithermal systems, where such a correlation usually characterizes the epithermal conditions. This is the case for the the Konos Hill prospect, where the concentrations of Au and As concentrations in pyrite is higher in the late, epithermal-stage.

Porphyry-style pyrite from both deposits, is generally enriched in trace elements compared to pyrite in from other porphyry deposits. Selenium in late, E-type pyrite from the Pagoni Rachi implies a genetic link and/or a constant evolution of the ore-forming system from the porphyry to the epithermal stage.

The composition of the studied pyrite generally follows the geochemical trends from other porphyry-epithermal systems, which reflects changes in the physico-chemical conditions of the ore forming fluids.

**Supplementary Materials:** The following are available online at <http://www.mdpi.com/2075-163X/10/9/784/s1>, Table S1: MASS-1, Table S2: EPMA data, Table S3: LA-ICP-MS data.

**Author Contributions:** Conceptualization, C.M.; methodology, S.K., J.B., A.T., and F.Z.; formal analysis, C.M., S.K., J.B., A.T., and F.Z.; data curation, C.M.; writing—original draft preparation, C.M.; writing—review and editing, C.M., P.V., P.G.S.; supervision, P.V., P.G.S., and V.M. All authors have read and agreed to the published version of the manuscript. The present study is part of the first author's PhD Thesis.

**Funding:** The first author (C.M.) would like to thank the Onassis Foundation, which granted him a scholarship for his PhD studies. A.T. was funded by CNRS-INSU (program CESSUR).

**Acknowledgments:** The authors would like to thank M. Keith, R. Klemd and K. Haase for providing comments on an earlier version of this manuscript. Beate Schmitte is kindly thanked for her kind help with the LA-ICP-MS analyses at the University of Münster, and Mr. Maik Zimmerman for his assistance with the EPM analyses at the University of Leoben. Two anonymous reviewers are thanked for providing constructive comments that improved the manuscript. T. Bornhorst is thanked for the editorial handling of the manuscript.

**Conflicts of Interest:** The authors declare no conflict of interest.

## References

1. Abraitis, P.K.; Patrick, R.A.D.; Vaughan, D.J. Variations in the compositional, textural and electrical properties of natural pyrite: A review. *Int. J. Miner. Process.* **2004**, *74*, 41–59. [[CrossRef](#)]
2. Cook, N.J.; Ciobanu, C.L.; Mao, J.W. Textural control on gold distribution in As-free pyrite from the Dongping, Huangtuliang, and Hougou gold deposits, North China craton (Hebei Province, China). *Chem. Geol.* **2009**, *264*, 101–121. [[CrossRef](#)]
3. Deditius, A.P.; Reich, M.; Kesler, S.E.; Utsunomiya, S.; Chryssoulis, S.L.; Walshe, J.; Ewing, R.C. The coupled geochemistry of Au and As in pyrite from hydrothermal ore deposits. *Geochim. Cosmochim. Acta* **2014**, *140*, 644–670. [[CrossRef](#)]
4. Keith, M.; Haase, K.M.; Klemd, R.; Krumm, S.; Strauss, S. Systematic variations of trace element and sulfur isotope compositions in pyrite with stratigraphic depth in the Skouriotissa volcanic-hosted massive sulfide deposit, Troodos ophiolite, Cyprus. *Chem. Geol.* **2016**, *423*, 7–18. [[CrossRef](#)]

5. Cook, N.J.; Chryssoulis, S.L. Concentrations of invisible gold in the common sulfides. *Can. Miner.* **1990**, *28*, 1–16.
6. Reich, M.; Deditius, A.; Chryssoulis, S.; Li, J.-W.; Ma, C.-Q.; Parada, M.A.; Barra, F.; Mittermayr, F. Pyrite as a record of hydrothermal fluid evolution in a porphyry copper system: A SIMS/EMPA trace element study. *Geochim. Cosmochim. Acta* **2013**, *104*, 42–62. [[CrossRef](#)]
7. Keith, M.; Häckel, F.; Haase, K.M.; Schwarz-Schampera, U.; Klemd, R. Trace element systematics of pyrite from submarine hydrothermal vents. *Ore Geol. Rev.* **2016**, *72*, 728–745. [[CrossRef](#)]
8. Reich, M.; Kesler, S.E.; Utsunomiya, S.; Palenik, C.S.; Chryssoulis, S.L.; Ewing, R.C. Solubility of gold in arsenian pyrite. *Geochim. Cosmochim. Acta* **2005**, *69*, 2781–2796. [[CrossRef](#)]
9. Kesler, S.E.; Deditius, A.P.; Chryssoulis, S. Geochemistry of Se and Te in arsenian pyrite: New evidence for the role of Se and Te hydrothermal complexes in Carlin and epithermal-type deposits. In *Au-Ag Telluride-Selenide Deposits: Field Workshop of IGCP-486, Espoo, Finland, 26–31 August 2007*; Kojonen, K.K., Cook, N.J., Ojala, V.J., Eds.; Geological Survey of Finland: Espoo, Finland, 2007; Volume 53, pp. 85–95.
10. Keith, M.; Smith, D.J.; Jenkin, G.R.T.; Holwell, D.A.; Dye, M.D. A review of Te and Se systematics in hydrothermal pyrite from precious metal deposits: Insights into ore forming processes. *Ore Geol. Rev.* **2018**, *96*, 269–282. [[CrossRef](#)]
11. Emsbo, P.; Hofstra, A.H.; Lauha, E.A.; Griffin, G.L.; Hutchinson, R.W.; John, D.A.; Theodore, T.G. Origin of high-grade gold ore, source of ore fluid components, and genesis of the Meikle and neighboring Carlin-type deposits, northern Carlin Trend, Nevada. *Econ. Geol.* **2003**, *98*, 1069–1105. [[CrossRef](#)]
12. Deditius, A.P.; Utsunomiya, S.; Reich, M.; Kesler, S.E.; Ewing, R.C.; Hough, R.; Walshe, J. Trace metal nanoparticles in pyrite. *Ore Geol. Rev.* **2011**, *42*, 32–46. [[CrossRef](#)]
13. Huston, D.L.; Sie, S.H.; Suter, G.F.; Cooke, D.R.; Both, R.A. Trace elements in sulfide minerals from Eastern Australian volcanic-hosted massive sulfide deposits: Part I. Proton microprobe analyses of pyrite, chalcopyrite and sphalerite, and part II. Selenium levels in pyrite: Comparison with d34S values and implications for the source of sulfur in volcanogenic hydrothermal systems. *Econ. Geol.* **1995**, *90*, 1167–1196.
14. Deditius, A.P.; Utsunomiya, S.; Renock, D.; Ewing, R.C.; Ramana, C.V.; Becker, U.; Kesler, S.E. A proposed new type of arsenian pyrite: Composition, nanostructure and geological significance. *Geochim. Cosmochim. Acta* **2008**, *72*, 2919–2933. [[CrossRef](#)]
15. Reich, M.; Becker, U. First-principles calculations of the thermodynamic mixing properties of arsenic incorporation into pyrite and marcasite. *Chem. Geol.* **2006**, *225*, 278–290. [[CrossRef](#)]
16. Blanchard, M.; Alfredsson, M.; Brodholt, J.; Wright, K.; Catlow, C.R.A. Arsenic incorporation into FeS<sub>2</sub> pyrite and its influence on dissolution: A DFT study. *Geochim. Cosmochim. Acta* **2007**, *71*, 624–630. [[CrossRef](#)]
17. Morey, A.A.; Tomkins, A.G.; Bierlin, F.P.; Wienberg, R.F.; Davidson, G.J. Bimodal distribution of gold in pyrite and arsenopyrite: Examples from the Archean Boorara and Bardoc shear systems, Yilgarn craton, Western Australia. *Econ. Geol.* **2008**, *103*, 599–614. [[CrossRef](#)]
18. Wohlgemuth-Ueberwasser, C.C.; Viljoen, F.; Petersen, S.; Vorster, C. Distribution and solubility limits of trace elements in hydrothermal black smoker sulfides: An insitu LA-ICP-MS study. *Geochim. Cosmochim. Acta* **2015**, *159*, 16–41. [[CrossRef](#)]
19. Franchini, M.; McFarlane, C.; Maydagán, L.; Reich, M.; Lentz, D.R.; Meinert, L.; Bouhier, V. Trace metals in pyrite and marcasite from the Agua Rica porphyry-high sulfidation epithermal deposit, Catamarca, Argentina: Textural features and metal zoning at the porphyry to epithermal transition. *Ore Geol. Rev.* **2015**, *66*, 366–387. [[CrossRef](#)]
20. Sykora, S.; Cooke, D.R.; Meffre, S.; Stephanov, A.S.; Gardner, K.; Scott, R.; Selley, D.; Harris, A.C. Evolution of pyrite trace element compositions from porphyry-style and epithermal conditions at the Lihir gold deposit: Implications for ore genesis and mineral processing. *Econ. Geol.* **2018**, *113*, 193–208. [[CrossRef](#)]
21. Goldfarb, R.J.; Baker, T.; Dubé, B.; Groves, D.I.; Hart, C.J.R.; Gosselin, P. Distribution, character and genesis of gold deposits in metamorphic terranes. *Econ. Geol.* **2005**, *100*, 407–450.
22. Sedorff, E.; Dilles, J.H.; Proffett, J.M.; Einaudi, M.T.; Zurcher, L.; Stavast, W.J.A.; Johnson, D.A.; Barton, M.D. Porphyry deposits: Characteristics and origin of hypogene features. *Econ. Geol.* **2005**, *100*, 251–298.
23. Simmons, S.F.; White, N.C.; John, D.A. Geological characteristics of epithermal precious and base metal deposits. *Econ. Geol.* **2005**, *100*, 485–522.

24. Revan, M.K.; Genç, Y.; Maslennikov, V.V.; Maslennikov, S.P.; Large, R.R.; Danyushevsky, L.V. Mineralogy and trace-element geochemistry of sulfide minerals in hydrothermal chimneys from the Upper-Cretaceous VMS deposits of the eastern Pontide orogenic belt (NE Turkey). *Ore Geol. Rev.* **2014**, *63*, 129–149. [[CrossRef](#)]
25. Foustoukos, D.I.; Seyfried, W.E. Fluid Phase Separation Processes in Submarine Hydrothermal Systems. In *Fluid–Fluid Interactions, Reviews in Mineralogy and Geochemistry*; Liebscher, A., Christoph, C.A., Eds.; Mineralogical Society of America: Chantilly, VA, USA, 2007; Volume 65, pp. 213–233.
26. Schmidt, K.; Koschinsky, A.; Garbe-Schönberg, D.; de Carvalho, L.M.; Seifert, R. Geochemistry of hydrothermal fluids from the ultramafic-hosted Logatchev hydrothermal field, 15° N on the Mid-Atlantic Ridge: Temporal and spatial investigation. *Chem. Geol.* **2007**, *242*, 1–21. [[CrossRef](#)]
27. Cook, N.J.; Ciobanu, C.L.; Spry, P.G.; Voudouris, P. Understanding gold-(silver)-telluride-(selenide) mineral deposits. *Episodes* **2009**, *32*, 249–263. [[CrossRef](#)]
28. Ciobanu, C.L.; Cook, N.J.; Pring, A.; Brugger, J.; Danyushevsky, L.V.; Shimizu, M. ‘Invisible gold’ in bismuth chalcogenides. *Geoch. Cosmoch. Acta* **2009**, *73*, 1970–1999. [[CrossRef](#)]
29. Deditius, A.P.; Utsunomiya, S.; Ewing, R.C.; Chryssoulis, S.L.; Venter, D.; Kesler, S.E. Decoupled geochemical behaviour of As and Cu in hydrothermal systems. *Geology* **2009**, *37*, 707–710. [[CrossRef](#)]
30. Maydagán, L.; Franchini, M.B.; Lentz, D.; Pons, J.; McFarlane, C. Sulfide composition and isotopic signature of the Altar Cu–Au deposit, Argentina: Constraints on the evolution of the porphyry–epithermal system. *Can. Miner.* **2013**, *51*, 813–840. [[CrossRef](#)]
31. Gregory, M.J.; Lang, J.R.; Gilbert, S.; Hoal, K.O. Geometallurgy of the Pebble porphyry copper–gold–molybdenum deposit, Alaska: Implications for gold distribution and paragenesis. *Econ. Geol.* **2013**, *108*, 463–482. [[CrossRef](#)]
32. Zwahlen, C.; Cioldi, S.; Wagner, T.; Rey, R.; Heinrich, C. The porphyry Cu–(Mo–Au) deposit at Altar (Argentina): Tracing gold distribution by vein mapping and LA–ICPMS mineral analysis. *Econ. Geol.* **2014**, *109*, 1341–1358. [[CrossRef](#)]
33. Alford, L.; Gysi, A.P.; Hurtig, N.C.; Monecke, T.; Pfaff, K. Porphyry-related polymetallic Au–Ag vein deposit in the Central City district, Colorado: Mineral paragenesis and pyrite trace element chemistry. *Ore Geol. Rev.* **2020**, *119*, 103295. [[CrossRef](#)]
34. Van Achtenbergh, E.; Ryan, C.G.; Jackson, S.E.; Griffin, W.L. Data reduction software for LA-ICP-MS: Appendix. In *Laser Ablation-ICP Mass Spectrometry in the Earth Sciences: Principles and Applications*; Sylvester, P.J., Ed.; Mineralogical Association Canada (MAC): Thunder Bay, ON, Canada, 2001; Volume 29, pp. 239–243.
35. Griffin, W.L.; Powell, W.J.; Pearson, N.J.; O’Reilly, S.Y. GLITTER: Data reduction software for laser ablation ICP-MS. In *Laser Ablation ICP-MS in the Earth Sciences: Current Practices and Outstanding Issues*; Sylvester, P., Ed.; Mineralogical Association of Canada: Thunder Bay, ON, Canada, 2008; Volume 40, pp. 308–311.
36. Jochum, K.P.; Nohl, U.; Herwig, K.; Lammel, E.; Stoll, B.; Hofmann, A.W. GeoReM: A New Geochemical Database for Reference Materials and Isotopic Standards. *Geost. Geoanal. Res.* **2005**, *29*, 333–338. [[CrossRef](#)]
37. Brun, J.-P.; Sokoutis, D. Core complex segmentation in North Aegean, a dynamic view. *Tectonics* **2018**, *37*, 1797–1830. [[CrossRef](#)]
38. Kydonakis, K.; Brunn, J.-P.; Sokoutis, D. North Aegean core complexes, the gravity spreading of a thrust wedge. *J. Geophys. Res. Solid Earth* **2015**, *120*, 1601. [[CrossRef](#)]
39. Kydonakis, K.; Moulas, E.; Chatzitheodoridis, E.; Brunn, J.-P.; Kostopoulos, D. First-report on Mesozoic eclogite-facies metamorphism preceding Barrovian overprint from the western Rhodope (Chalkidiki, northern Greece). *Lithos* **2015**, *220*, 147–163. [[CrossRef](#)]
40. Turpaud, P.; Reischmann, T. Characterisation of igneous terranes by zircon dating: Implications for UHP occurrences and suture identification in the Central Rhodope, northern Greece. *Int. J. Earth Sci.* **2010**, *99*, 567–591. [[CrossRef](#)]
41. Magganas, A.C. Constraints on the petrogenesis of Evros ophiolite extrusives, NE Greece. *Lithos* **2002**, *65*, 165–182. [[CrossRef](#)]
42. Bonev, N.; Marchev, P.; Moritz, R.; Collings, D. Jurassic subduction zone tectonics of the Rhodope Massif in the Thrace region (NE Greece) as revealed by new U–Pb and <sup>40</sup>Ar/<sup>39</sup>Ar geochronology of the Evros ophiolite and high-grade basement rocks. *Gondwana Res.* **2015**, *27*, 760–775. [[CrossRef](#)]
43. Jolivet, L.; Faccenna, C.; Huet, B.; Labrousse, L.; Le Pourhiet, L.; Lacombe, O.; Lecomte, E.; Burov, E.; Denèle, Y.; Brun, J.-P.; et al. Aegean tectonics: Strain localization, slab tearing and trench retreat. *Tectonophysics* **2013**, *597*, 1–33. [[CrossRef](#)]

44. Kiliyas, A.; Falalakis, G.; Sfeikos, A.; Papadimitriou, E.; Vamvaka, A.; Gkarlaouni, C. The Thrace basin in the Rhodope province of NE Greece—A Tertiary supra-detachment basin and its geodynamic implications. *Tectonophysics* **2013**, *595*, 90–105. [[CrossRef](#)]
45. Del Moro, A.; Innocenti, F.; Kyriakopoulos, C.; Manetti, P.; Papadopoulos, P. Tertiary granitoids from Thrace (Northern Greece): Sr isotopic and petrochemical data. *Neues Jahrbuch für Mineralogie Abhandlungen* **1988**, *159*, 113–115.
46. Marchev, P.; Kaiser-Rohrmeier, B.; Heinrich, C.; Ovtcharova, M.; von Quadt, A.; Raicheva, R. Hydrothermal ore deposits related to post-orogenic extensional magmatism and core complex formation: The Rhodope Massif of Bulgaria and Greece. *Ore Geol. Rev.* **2005**, *27*, 53–89. [[CrossRef](#)]
47. Perkins, R.; Copper, F.J.; Condon, D.J.; Tattitsch, B.; Naden, J. Post-collisional Cenozoic extension in the northern Aegean: The high-K to shoshonitic intrusive rocks of the Maronia Magmatic Corridor, northeastern Greece. *Lithosphere* **2018**, *10*, 582–601. [[CrossRef](#)]
48. Voudouris, P.; Tarkian, M.; Arikas, K. Mineralogy of telluride-bearing epithermal ores in Kassiteres-Sappes area, western Thrace, Greece. *Miner. Petol.* **2006**, *87*, 31–52. [[CrossRef](#)]
49. Mavrogonatos, C.; Voudouris, P.; Spry, P.G.; Melfos, V.; Klemme, S.; Berndt, J.; Baker, T.; Moritz, R.; Bissig, T.; Monecke, T.; et al. Mineralogical Study of the Advanced Argillic Alteration Zone at the Konos Hill Mo–Cu–Re–Au Porphyry Prospect, NE Greece. *Minerals* **2018**, *8*, 479. [[CrossRef](#)]
50. Pe-Piper, G.; Piper, D.J.W. The igneous rocks of Greece: The anatomy of an orogen. In *Beiträge der Regionalen Geologie der Erde*; Gebrüder Borntraeger: Berlin, Germany, 2002; p. 573.
51. Moritz, R.; Márton, I.; Ortelli, M.; Marchev, P.; Voudouris, P.; Bonev, N.; Spikings, R.; Cosca, M. A review of age constraints of epithermal precious and base metal deposits of the Tertiary Eastern Rhodopes: Coincidence with Late Eocene–Early Oligocene tectonic plate reorganization along the Tethys. In *Scientific Annals of the School of Geology AUTH, Proceedings of the XIX Congress of the Carpathian Balkan Geological Association, Thessaloniki, Greece, 23–26 September 2010*; Christofides, G., Kantiranis, D., Kostopoulos, D.S., Chatzipetros, A., Eds.; Faculty of Sciences, Aristotle University of Thessaloniki: Solun, Greece, 2010; Volume 100, pp. 351–358.
52. Ersoy, E.Y.; Palmer, M.R. Eocene–Quaternary magmatic activity in the Aegean: Implications for mantle metasomatism and magma genesis in an evolving orogeny. *Lithos* **2013**, *180*, 5–24. [[CrossRef](#)]
53. Arikas, K.; Voudouris, P. Hydrothermal alterations and mineralizations of magmatic rocks in the southern Rhodope Massif. *Acta Volcanol.* **1998**, *10*, 353–365.
54. Melfos, V.; Voudouris, P. Cenozoic metallogeny of Greece and potential for precious, critical and rare metals exploration. *Ore Geol. Rev.* **2017**, *59*, 1030–1057. [[CrossRef](#)]
55. Voudouris, P.; Mavrogonatos, C.; Spry, P.G.; Baker, T.; Melfos, V.; Klemm, R.; Haase, K.; Repstock, A.; Djiba, A.; Bismayer, U.; et al. Porphyry and epithermal deposits in Greece: An overview, new discoveries, and mineralogical constraints on their genesis. *Ore Geol. Rev.* **2019**, *107*, 654–691. [[CrossRef](#)]
56. Tsirambides, A.; Filippidis, A. Sb–Bi–Bearing Metallogeny of the SerboMacedonian–Rhodope Metallogenic Belt (SRMB). *Bull. Geol. Soc. Greece* **2019**, *55*, 34–64. [[CrossRef](#)]
57. Galanopoulos, E.; Voudouris, P.; Mavrogonatos, C.; Spry, P.G.; Hart, C.; Melfos, V.; Zaccarini, F.; Alfieris, D.A. New porphyry Mo mineralization at Aisymi–Leptokarya, South-Eastern Rhodope, North-East Greece: Geological and mineralogical constraints. *Geosciences* **2018**, *8*, 435. [[CrossRef](#)]
58. Melfos, V.; Vavelidis, M.; Christofides, G.; Seidel, E. Origin and evolution of the Tertiary Maronia porphyry copper–molybdenum deposit, Thrace, Greece. *Miner. Depos.* **2002**, *37*, 648–668. [[CrossRef](#)]
59. Melfos, V.; Voudouris, P.; Melfou, M.; Sánchez, M.G.; Papadopoulou, L.; Filippidis, A.; Spry, P.G.; Schaarschmidt, A.; Klemm, R.; Haase, K.M.; et al. Mineralogical constraints on the potassic and sodic–calcic hydrothermal alteration and vein-type mineralization of the Maronia porphyry Cu–Mo ± Re ± Au deposit in NE Greece. *Minerals* **2020**, *10*, 182. [[CrossRef](#)]
60. Ortelli, M.; Moritz, R.; Voudouris, P.; Spangenberg, J. Tertiary porphyry and epithermal association of the Sapes–Kassiteres district, Eastern Rhodopes, Greece. In *Proceedings of the 10th Biennial SGA Meeting, Townsville, Australia, 17–20 August 2009*; pp. 536–538.
61. Voudouris, P. Hydrothermal corundum, topaz, diaspore and alunite supergroup minerals in the advanced argillic alteration lithocap of the Kassiteres–Sapes porphyry–epithermal system, western Thrace, Greece. *J. Miner. Geochem.* **2014**, *191*, 117–136. [[CrossRef](#)]

62. Mavrogonatos, C.; Voudouris, P.; Spry, P.G.; Melfos, V.; Klemme, S.; Berndt, J.; Moritz, R.; Kanellopoulos, C. First zunyite-bearing lithocap in Greece: The case of Konos Hill Mo-Re-Cu-Au porphyry system. In Proceedings of the 1st International Electronic Conference on Mineral Science, Sciforum, Basel, Switzerland, 16–31 July 2018; Volume 1. [\[CrossRef\]](#)
63. Voudouris, P.; Melfos, V.; Spry, P.G.; Bindi, L.; Kartal, T.; Arikas, K.; Moritz, R.; Ortelli, M. Rhenium-rich molybdenite and rheniite (ReS<sub>2</sub>) in the Pagoni Rachi-Kirki Mo-Cu-Te-Ag-Au deposit, Northern Greece. implications for the rhenium geochemistry of porphyry style Cu-Mo and Mo mineralization. *Can. Miner.* **2009**, *47*, 1013–1036. [\[CrossRef\]](#)
64. Voudouris, P.; Melfos, V.; Spry, P.G.; Bindi, L.; Moritz, R.; Ortelli, M.; Kartal, T. Extremely Re-rich molybdenite from porphyry Cu-Mo-Au prospects in northeastern Greece: Mode of occurrence, causes of enrichment, and implications for gold exploration. *Minerals* **2013**, *3*, 165–191. [\[CrossRef\]](#)
65. Voudouris, P.; Melfos, V.; Spry, P.G.; Kartal, T.; Schleicher, H.; Moritz, R.; Ortelli, M. The Pagoni Rachi/Kirki Cu-Mo-Re-Au-Ag-Te deposit, northern Greece: Mineralogical and fluid inclusion constraints on the evolution of a telescoped porphyry-epithermal system. *Can. Miner.* **2013**, *51*, 411–442. [\[CrossRef\]](#)
66. Mavrogonatos, C.; Voudouris, P.; Berndt, J.; Klemme, S.; Zaccarini, F.; Spry, P.G.; Melfos, V.; Tarantola, A.; Keith, M.; Klemd, R.; et al. Trace Elements in Magnetite from the Pagoni Rachi Porphyry Prospect, NE Greece: Implications for Ore Genesis and Exploration. *Minerals* **2019**, *9*, 725. [\[CrossRef\]](#)
67. Mavrogonatos, C.; Voudouris, P.; Spry, P.G.; Melfos, V.; Klemme, S.; Berndt, J.; Periferakis, A. Biotite Chemistry from Porphyry-Style Mineralization in Western Thrace, Greece. In Proceedings of the 8th Geochemistry Symposium, Antalya, Turkey, 2–6 May 2018; Volume 193, pp. 2–6.
68. Kiliass, S.P.; Naden, J.; Paktsevanoglou, M.; Giampouras, M.; Stavropoulou, A.; Apeiranthiti, D.; Mitsis, I.; Koutles, T.; Michael, K.; Christidis, C. Multistage alteration, mineralization and ore-forming fluid properties at the Viper (Sappes) Au–Cu–Ag–Te ore body, W. Thrace, Greece. *Bull. Geol. Soc. Greece* **2013**, *47*, 1635–1644. [\[CrossRef\]](#)
69. Voudouris, P.; Melfos, V.; Spry, P.G.; Baker, T. Cenozoic Porphyry-Epithermal and Other Intrusion-Related Deposits in Northeastern Greece: Geological, Mineralogical and Geochemical Constraints. *Soc. Econ. Geol. Guide Ser.* **2016**, *54*, 43–82.
70. Voudouris, P.; Melfos, V.; Baker, T.; Spry, P.G. Diverse Styles of Oligocene-Miocene Magmatic-Hydrothermal Deposits in Northeastern Greece: Relationships between Tectonic-, Magmatic Activity, Alteration and Au-Ag Mineralization. *Soc. Econ. Geol. Guide Ser.* **2016**, *54*, 83–112.
71. Voudouris, P.; Melfos, V.; Spry, P.G.; Moritz, R.; Papavassiliou, K.; Falalakis, G. Mineralogy and geochemical environment of formation of the Perama Hill high-sulfidation epithermal Au-Ag-Te-Se deposit, Petrotta Graben, NE Greece. *Miner. Petrol.* **2011**, *103*, 79–100. [\[CrossRef\]](#)
72. Repstock, A.; Voudouris, P.; Kolitsch, U. New occurrences of watanabeite, colusite, “arsenosulvanite” and Cu-excess tetrahedrite-tennantite at the Pefka high-sulfidation epithermal deposit, northeastern Greece. *J. Miner. Geochem.* **2015**, *192*, 135–149. [\[CrossRef\]](#)
73. Ortelli, M.; Moritz, R.; Voudouris, P.; Cosca, M.; Spangenberg, J. Tertiary porphyry and epithermal association of the Sapes-Kassiteres district, Eastern Rhodopes, Greece. In Proceedings of the 8th Swiss Geoscience Meeting, Fribourg, Switzerland, 19–20 November 2010.
74. Voudouris, P.; Mavrogonatos, C.; Melfos, V.; Spry, P.G.; Magganas, A.; Alfieris, D.; Soukis, K.; Tarantola, A.; Periferakis, A.; Kołodziejczyk, J.; et al. The geology and mineralogy of the Stypsi porphyry Cu-Mo-Au-Re prospect, Lesbos Island, Aegean Sea, Greece. *Ore Geol. Rev.* **2019**, *112*, 10323. [\[CrossRef\]](#)
75. Arancibia, O.N.; Clark, A.H. Early magnetite–amphibole–plagioclase alteration–mineralization in the Island Copper porphyry copper–gold–molybdenum deposit, British Columbia. *Econ. Geol.* **1996**, *91*, 402–438. [\[CrossRef\]](#)
76. Gustafson, L.B.; Hunt, J.P. The porphyry copper deposit at El Salvador, Chile. *Econ. Geol.* **1975**, *70*, 857–912. [\[CrossRef\]](#)
77. Masterman, G.J.; Cooke, D.R.; Berry, R.F.; Walshe, J.L.; Lee, A.W.; Clark, A.H. Fluid chemistry, structural setting, and emplacement history of the Rosario Cu-Mo porphyry and Cu-Ag-Au epithermal veins, Collahuasi district, northern Chile. *Econ. Geol.* **2005**, *100*, 835–862. [\[CrossRef\]](#)
78. Monecke, T.; Monecke, J.; Reynolds, T.J.; Tsuruoka, S.; Bennett, M.M.; Skewes, W.B.; Palin, R.M. Quartz solubility in the H<sub>2</sub>O–NaCl System: A framework for understanding vein formation in porphyry copper deposits. *Econ. Geol.* **2018**, *113*, 1007–1046. [\[CrossRef\]](#)

79. Fouquet, Y.; Henry, K.; Knott, R.; Cambon, P. Geochemical Section of the TAG Hydrothermal Mound. *Proc. Ocean Drill. Program Sci. Results* **1998**, *158*, 363–387.
80. Ding, K.; Seyfried, W.E. Determination of Fe–Cl complexing in the low pressure supercritical region (NaCl fluid): Iron solubility constraints on pH of seafloor hydrothermal fluids. *Geochim. Cosmochim. Acta* **1992**, *56*, 3681–3692. [[CrossRef](#)]
81. Bazarkina, E.F.; Pokrovski, G.S.; Zotov, A.V.; Hazemann, J.-L. Structure and stability of cadmium chloride complexes in hydrothermal fluids. *Chem. Geol.* **2010**, *276*, 1–17. [[CrossRef](#)]
82. Pokrovski, G.S.; Borisova, A.Y.; Bychkov, A.Y. Speciation and Transport of Metals and Metalloids in Geological Vapors. In *Thermodynamics of Geothermal Fluids, Reviews in Mineralogy and Geochemistry*; Stefánsson, A., Driesner, T., Bénézeth, P., Eds.; Mineralogical Association Canada (MAC): Thunder Bay, ON, Canada, 2013; Volume 76, pp. 165–218.
83. Layton-Matthews, D.; Peter, J.M.; Scott, S.D.; Leybourne, M. Distribution, mineralogy, and geochemistry of selenium in felsic volcanic-hosted massive sulfide deposits of the Finlayson Lake district, Yukon Territory, Canada. *Econ. Geol.* **2008**, *103*, 61–88. [[CrossRef](#)]
84. Kesler, S.E.; Chryssoulis, S.L.; Simon, G. Gold in porphyry copper deposits: Its abundance and fate. *Ore Geol. Rev.* **2002**, *21*, 103–124. [[CrossRef](#)]
85. Pokrovski, G.S.; Zakirov, I.V.; Roux, J.; Testemale, D.; Hazemann, J.L.; Bychkov, A.V.; Golikova, G.V. Experimental study of arsenic speciation in vapor phase to 500 °C: Implications for As transport and fractionation in low-density crustal fluids and volcanic gases. *Geochim. Cosmochim. Acta* **2002**, *66*, 3453–3480. [[CrossRef](#)]
86. Pokrovski, G.S.; Roux, J.; Harrichoury, J.C. Fluid density control on vapor–liquid partitioning of metals in hydrothermal systems. *Geology* **2005**, *33*, 657–660. [[CrossRef](#)]
87. Williams-Jones, A.E.; Heinrich, C.A. Vapor transport of metals and the formation of magmatic-hydrothermal ore deposits. *Econ. Geol.* **2005**, *100*, 1287–1312. [[CrossRef](#)]
88. Klemm, L.M.; Pettke, T.; Heinrich, C.A.; Campos, E. Hydrothermal evolution of the El Teniente deposit, Chile: Porphyry Cu–Mo ore deposition from low-salinity magmatic fluids. *Econ. Geol.* **2007**, *102*, 1021–1045. [[CrossRef](#)]
89. Simon, A.C.; Pettke, T.; Candela, P.A.; Piccoli, P.M.; Heinrich, C.A. The partitioning behaviour of As and Au in S-free and S-bearing magmatic assemblages. *Geochim. Cosmochim. Acta* **2007**, *71*, 1764–1782. [[CrossRef](#)]
90. Voudouris, P.; Spry, P.G.; Melfos, V.; Haase, K.; Klemm, R.; Mavrogenatos, C.; Repstock, A.; Alfieris, D. Gold deposits in Greece: Hypogene ore mineralogy as a guide for precious and critical metal exploration. In Proceedings of the 1st International Electronic Conference on Mineral Science, Basel, Switzerland, 16–31 July 2018; p. 13. [[CrossRef](#)]
91. Voudouris, P.; Spry, P.G.; Melfos, V.; Alfieris, D. Tellurides and bismuth sulfosalts in gold occurrences of Greece: Mineralogy and genetic considerations. *Geol. Surv. Finland Guide* **2007**, *53*, 85–94.
92. Voudouris, P. A comparative mineralogical study of Te-rich magmatic-hydrothermal systems in northeastern Greece. *Miner. Petrol.* **2006**, *87*, 241–275. [[CrossRef](#)]
93. Melfos, V.; Voudouris, P. Geological, mineralogical and geochemical aspects for critical and rare metals in Greece. *Minerals* **2012**, *2*, 300–317. [[CrossRef](#)]

